

Measurement of high p_T K_S^0 mesons
in Au+Au collisions at $\sqrt{s_{NN}} = 200\text{GeV}$

Yoshihiro Iwanaga
(M072348)

Graduate School of Science
HIROSHIMA UNIVERSITY

February 10, 2009

Abstract

The PHENIX experiment at the Relativistic Heavy Ion Collider (RHIC) has shown a strong suppression of the yield of hadrons at Au+Au collisions^{1 2}. In addition, same magnitude of the suppression is observed for η and π^0 mesons, with independent of their hadron mass³. This result is successfully re-produced by the GLV parton energy-loss model, which is based on a scenario that high energy partons lose their energy by gluon radiation as they traverse a hot and dense medium formed in the ultra-relativistic nuclear collisions⁴.

However, the experiments at RHIC have provided new puzzles. The results suggest that quark number or flavor may be sensitive to energy loss in the medium⁵. By measuring mesons including heavier quark at transverse momentum (p_T) above 5 GeV/c, we can judge whether the flavor dependence of parton energy loss exists or not because other effect such as quark-recombination become negligible at sufficiently high p_T .

In this analysis, I measured K_S^0 mesons, that include strangeness quark, via $K_S^0 \rightarrow 2\pi^0 \rightarrow 4\gamma$ decay mode. This decay mode is only way to measure high p_T K_S^0 mesons since the particle tracking detectors installed in PHENIX can measure mesons of p_T up to 5 GeV/c. But on the other hand, this measurement is very challenging because of the huge combinatorial background for reconstructing. To minimize background, I introduced a new parameter for particle identification based on the phase-space distribution of $K^0 \rightarrow \pi^0\pi^0$ decay. In addition, cut parameters for π^0 meson identification are optimized. Finally, I succeeded in measuring high p_T K_S^0 mesons produced in heavy ion collisions at RHIC.

I report invariant yield of K_S^0 mesons measured in Au+Au collisions at $\sqrt{s_{NN}} = 200\text{GeV}$ as a function of p_T . Furthermore, I qualified medium effect by the nuclear modification factor, which is defined as the ratio of K_S^0 yeild in Au+Au and p+p collisions scaled by the number of binary nucleon collisions, and discussed more detailed mechanism of the partonic interaction.

¹S. S. Adler *et al.* Phys. Rev. Lett. **96**, 202301 (2006).

²K. Adcox *et al.* Phys. Rev. Lett. **88**, 022301 (2002).

³S. S. Adler *et al.* Phys. Rev. Lett. **96**, 202301 (2006).

⁴M. Gyulassy, P. Levai and I. Vitev, Phys. Lett. **594**, 371 (2001).

⁵J. Phys. G: Nucl. Part. Phys. **35** (2008) 104158

Contents

1	Introduction	8
1.1	Perturbative Quantum Chromo-Dynamics	8
1.1.1	Quarks and Leptons	8
1.1.2	QCD Lagrangian	9
1.1.3	Asymptotic Freedom and Confinement	9
1.1.4	Quark Gluon Plasma(QGP)	10
1.2	Parton Energy Loss	11
1.2.1	LPM Effect and Gluon Radiation	11
1.2.2	Parton Energy Loss Models	12
1.2.3	Recent Results	13
2	Experimental Setup	14
2.1	RHIC Accelerator	14
2.2	PHENIX Detector	16
2.2.1	Global Detectors	17
2.2.2	Central Spectrometer	19
2.2.3	Electro Magnetic Calorimeter	24
2.2.4	Muon Arm Detectors	29
2.3	Data Acquisition (DAQ) System	30
2.3.1	DAQ Overview	30
2.3.2	Front-end Electronics Module	31
2.3.3	Data Collection Module	32
2.3.4	Event Builder	32
2.3.5	Level-1 Trigger	33
2.3.6	Level-2 Trigger	33
3	Analysis	34
3.1	Data Set	34

3.1.1	Trigger Selection	34
3.1.2	Run by Run Quality Assurance	35
3.2	Centrality Determination	36
3.3	Signal Selection	37
3.3.1	Photon Identification	37
3.3.2	π^0 Identification	40
3.3.3	K_S^0 Identification	44
3.3.4	Peak Extraction	46
3.4	Simulation	56
3.4.1	Event Generator	56
3.4.2	Detector Simulation	56
3.4.3	Multiplicity Effect Simulation	58
3.4.4	Inclusive Detection Efficiency	60
4	Invariant Yield and Cross Section	63
4.1	Introduction	63
4.2	Invariant Yield	64
4.3	Bin Shift Correction	64
5	Systematic Errors	65
5.1	Peak Extraction	65
5.1.1	Geometrical Acceptance of the EMCal	65
5.1.2	Energy Scale and Nonlinearity	65
5.1.3	Conversion	66
5.1.4	Branching Ratio	66
5.2	Summary of Systematic Errors	66
6	Results and Discussion	68
6.1	K_S^0 Spectra	68
6.2	Medium Effect on K_S^0 meson in Au+Au Collisions at $\sqrt{s_{NN}} = 200$ GeV	70
6.2.1	Nuclear Modification Factor	70
6.2.2	Comparison with Other Mesons	72
6.2.3	Comparison with Theoretical Predictions	74
7	Conclusion	76
	Acknowledgement	77

A Kinematics	78
A.1 Coordinate	78
A.2 Kinematic Variables	79
B Basic Constants of K_S^0 meson	81
C $d^2N/dp_T dy$	82
D List of Analyzed Runs	84

List of Figures

1.1	Schetch of the QCD phase diagram	11
1.2	Nuclear modification factor R_{AA} of different mesons ($\pi^0, \eta, \phi, \omega, J/\psi$) and direct photons at midrapidity	13
2.1	Schematic view of the RHIC complex	14
2.2	RHIC intersection points	16
2.3	Location of the PHENIX subsystems	17
2.4	The position of BBC	18
2.5	Schematic view of the PHENIX magnet system. Arrows indicates the beam direction.	19
2.6	Megnetic field lines for ++ mode	20
2.7	Construction of DC frame	21
2.8	Schematic operation of the TEC	22
2.9	Schematic view of the component of a single TOF panel	23
2.10	Overview of one module of the PbSc EMCal	26
2.11	Energy liniarity by beam tests at BNL (left) and CERN (right). The solid lines show total systematic uncertainties in the analysis	27
2.12	PbSc timing resolution for different particles. Top:timing distribution for 1 GeV/c electrons, pions and protons. Bottom:timing resolution in the momentum rage of 0.3 - 1.0 GeV/c.	28
2.13	Interior view of one PbGl supermodule	29
2.14	Sketch of the PHENIX online system	31
2.15	Block diagram of Front-end Electronics Module	32
3.1	Distribution of collision vertex measured by BBC. This distribution is obtained through the online vertex selection by BBLL1.	34
3.2	Run by run peak positions of π^0 invariant mass	35
3.3	Run by run width of π^0 invariant mass	35
3.4	Sketch of correlation between signal amount and centrality	37

3.5	Total ZDC signal versus total charge measured by the BBC. Division into different centrality classes is based on this distribution.	37
3.6	Shower shape for hadronic shower (left) and electromagnetic shower (right).	38
3.7	χ^2 distribution for showers induced by 2 GeV/c electrons and pions.	39
3.8	Time of flight distributions for photons from vertex and not from vertex, and non-photons obtained by simulation. The black line is obtained by minimum bias event.	40
3.10	Energy asymmetry of photon pairs with $3\text{GeV}/c \leq p_T \leq 5\text{GeV}/c$ from π^0 within the one sector acceptance (simulated) and measured within minimum bias events.	43
3.11	Distribution of cluster energy measured in minimum bias events	43
3.12	Geometrical acceptance for π^0 requiring both photons detected in the same EMCal sector.	45
3.13	centrality and momentum dependence of mass peak position	46
3.14	Invariant mass spectra for $5.5 \leq p_T < 6.5$ GeV/c, minimum bias event . . .	47
3.15	Invariant mass spectra for $6.5 \leq p_T < 7.5$ GeV/c, minimum bias event . . .	48
3.16	Invariant mass spectra for $7.5 \leq p_T < 8.5$ GeV/c, minimum bias event . . .	49
3.17	Invariant mass spectra for $8.5 \leq p_T < 9.5$ GeV/c, minimum bias event . . .	50
3.18	Invariant mass spectra for $9.5 \leq p_T < 10.5$ GeV/c, minimum bias event . .	51
3.19	Invariant mass spectra for $10.5 \leq p_T < 11.5$ GeV/c, minimum bias event .	52
3.20	Invariant mass spectra for $2.5 \leq p_T < 3.5$ GeV/c, centrality 60-92.2% . . .	53
3.21	Invariant mass spectra for $3.5 \leq p_T < 4.5$ GeV/c, centrality 60-92.2% . . .	54
3.22	Invariant mass spectra for $5.5 \leq p_T < 5.5$ GeV/c, centrality 60-92.2% . . .	55
3.23	An event display of $K_S^0 \rightarrow \pi^+ \pi^-$ decay. This decay is processed in PISA. .	57
3.24	An event display of $K_S^0 \rightarrow 2\pi^0 \rightarrow 4\gamma$ decay. This decay is processed in PISA.	57
3.25	Main program flow of the embedding algorithm.	59
3.26	Geometrical and reconstruction efficiency calculated by embedding simulation (Centrality 0-92.2%)	60
3.27	Geometrical and reconstruction efficiency calculated by embedding simulation (Centrality 60-92.2%)	61
3.9	2γ mass spectra sliced by centrality	62
6.1	Invariant yield of K_S^0 in Au+Au Collisions at $\sqrt{s_{NN}} = 200$ GeV (Minimum Bias)	69
6.2	Invariant yield of K_S^0 in peripheral collisions (centrality:60-92.2%)	69
6.3	Nuclear modification factor of K_S^0 in Au+Au collisions at $\sqrt{s} = 200$ GeV .	71

6.4	Nuclear modification factor of K_S^0 in Au+Au peripheral collisions at $\sqrt{s} = 200$ GeV	71
6.5	Comparison of nuclear modification factors in Au+Au $\sqrt{s} = 200$ GeV collisions (Centrality 0-92.2%)	73
6.6	R_{AA} of mesons as a function of p_T . The black line represents GLV model calculation using gluon density $dN_g/dy = 1150$	74
6.7	Prediction of nuclear modification factor for K_S^0 at $\sqrt{s_{NN}} = 200$ GeV Au+Au collisions with and without jet conversion effect.	75
A.1	Coordinate system of the PHENIX experiment	78
C.1	p_T spectra in centrality 0-92.2%	82
C.2	p_T spectra in peripheral collisions	83

List of Tables

2.1	Basic parameters of two kinds of PHENIX EMCAL	25
3.1	Centrality dependence of π^0 mass position and width. With increasing centrality, reconstructed mass shifts higher.	41
5.1	Summary of systematic errors. Shown values are % unit.	67
B.1	Basic constants of K_S^0	81
D.1	List of Analyzed Runs	85

Chapter 1

Introduction

1.1 Perturbative Quantum Chromo-Dynamics

1.1.1 Quarks and Leptons

The start line of the quark model was marked by the introduction of new quantum number, named as “*strangeness*” by Gell-Mann and Nishijima in 1953. In 1956, S.Sakata group introduced a similar model with a different quantum coordination. At this time, no one thought the new quantum number is related to the structure of nucleon. Many new particles with *strangeness number* were discovered on the accelerators; Bevatron at Lawrence Berkeley National Laboratory, Cosmotron and AGS¹ at Brookhaven National Laboratory.

The SU(3) hadron model was introduced by Gell-Mann and Ne’eman in 1961 in order to categorize the new strangeness particles and this model was a first trigger to understand the structure of the nucleon. The concept of quark was introduced by Gell-Mann in 1964 and the concept of gluon with the idea of color charge was introduced by Nambu, Han and Greenberg in 1965. They were baseline of the Quantum Chromo-Dynamics(QCD) theory introduced in 1973[8]. Due to the color force, the quark and gluon deconfined inside the hadron.

The first experimental evidence of the constituent parton in proton was reported in deep inelastic scattering at Stanford Linear Accelerator Center. About 25 years later of the first discovery, the top quark was discovered in $p + p$ collisions at Tevatron in Fermi National Accelerator Laboratory.

¹Alternating Gradient Synchrotron

1.1.2 QCD Lagrangian

Quantum Chromodynamics (QCD) is the gauge field theory which describes the strong interactions of colored quarks and gluons. This theory is one of the components of the Standard Model. The quarks have a specific flavor and one color of the three, red, green and blue. The gluons have a color of eight. The hadrons are the state which is color singlet of quarks, anti-quarks and gluons. The QCD Lagrangian is described as follows;

$$L_{QCD} = -\frac{1}{4}F_{\mu\nu}^{(a)}F^{(a)\mu\nu} + i \sum_q \bar{\phi}_q^i \gamma^\mu (D_\mu)_{ij} \phi_q^j - \sum_q m_q \bar{\phi}_q^i \phi_{qi} \quad (1.1)$$

$$F_{\mu\nu}^{(a)} = \partial_\mu A_\nu^a - \partial_\nu A_\mu^a - g_s f_{abc} A_\mu^b A_\nu^c \quad (1.2)$$

$$(D_\mu)_{ij} = \delta_{ij} \partial_\mu + i g_s \sum_a \frac{\lambda_{i,j}^a}{2} A_\mu^a \quad (1.3)$$

where the $\phi_q^i(x)$ are the 4-component Dirac spinors associated with the field of the each quark of color i and flavor q . The $A_\mu^a(x)$ are the gluon (Yung-Mills) fields. The g_s is the QCD coupling constant and the f_{abc} are the structure constants of the SU(3) algebra. In the equation 1.1, the first term $\frac{1}{4}F_{\mu\nu}^{(a)}F^{(a)\mu\nu}$ corresponds to the free gluon field, the second term $i \sum_q \bar{\phi}_q^i \gamma^\mu (D_\mu)_{ij} \phi_q^j$ corresponds to the interaction of quark in the gluon field and the last term $\sum_q m_q \bar{\phi}_q^i \phi_{qi}$ corresponds to the free quarks of mass m_q in a rest state. m_q represents the diagonal matrix of current masses,

$$m_q = \begin{pmatrix} m_u & & & \\ & m_d & & \\ & & m_s & \\ & & & \ddots \end{pmatrix} \quad (1.4)$$

which are parameters the Standard Model. With $m_u, m_d, m_s \simeq 4, 7, 150$ MeV and $m_c, m_b, m_t \simeq 1.5, 4.5, 175$ GeV. The Feynman rules are derived from this Lagrangian.

1.1.3 Asymptotic Freedom and Confinement

The QCD describes the strong interaction successfully, which is characterized by the following two features. One is the asymptotic freedom and the other is the confinement. The renormalization scale dependence of the effective QCD coupling constant $\alpha_s = g_s^2/4\pi$ is controlled by β -function as follows.

$$\mu \frac{\partial \alpha_s}{\partial \mu} = 2\beta(\alpha_s) = -\frac{\beta_0}{2\pi} \alpha_s^2 - \frac{\beta_1}{4\pi} \alpha_s^3 - \frac{\beta_2}{64\pi} \alpha_s^4 - \dots$$

$$\beta_0 = 11 - \frac{2}{3} n_f,$$

$$\beta_1 = 51 - \frac{19}{3}n_f,$$

$$\beta_2 = 2857 - \frac{5033}{9}n_f + \frac{325}{27}n_f^2$$

where μ is a renormalization scale, n_f is the number of quark flavor, g_s is the color charge. The solution of this equation is expressed as an expansion in inverse powers of $\ln(\mu^2)$ as follows.

$$\alpha_s = \frac{4\pi}{\beta_0 \ln(\mu^2/\Lambda^2)} \left[1 - \frac{2\beta_1}{\beta_0^2} \frac{\ln[\ln(\mu^2/\Lambda^2)]}{\ln(\mu^2/\Lambda^2)} + \frac{4\beta_1^2}{\beta_0^4 \ln^2(\mu^2/\Lambda^2)} \left(\left(\ln[\ln(\mu^2/\Lambda^2)] - \frac{1}{2} \right)^2 + \frac{\beta_2\beta_0}{8\beta_1^2} - \frac{5}{4} \right) \right]$$

where Λ is the scale parameter in QCD. It is clear that this equation approaches to 0 when μ^2 increases to infinity. This means that when two quarks are in vicinity each other, the strong force becomes relatively weak. On the other hand, when two quarks are spatially distant, the force becomes strong. At a distance, it becomes easier to produce a pair of quark and anti-quark rather than keeping the distance between the quarks against the interacting force. The created quark and anti-quark form a hadron and this is called as “deconfinement”. The weakness of this interaction at short distance is called as “asymptotic freedom”. Because of the asymptotic freedom, the QCD quantity, such as cross section σ , can be calculated using perturbation method as follows.

$$\sigma = c_1\alpha_s + c_2\alpha_s^2 + c_3\alpha_s^3 + \dots$$

where c_i ($i = 1, 2, \dots$) come from calculating the appropriate Feynman diagrams. Such method is called perturbative Quantum Chromo-Dynamics (pQCD). The pQCD is applicable to the QCD quantity when μ^2 is more than 1 GeV. Due to the confinement, single quark cannot be extracted from hadrons.

1.1.4 Quark Gluon Plasma(QGP)

Quarks are confined inside hadron as discussed in Section 1.1.3. A nuclear matter is heated and compressed, hadrons occupy more and more of the available space. Eventually they start to overlap and the initially confined quarks and gluons begin to percolate between the hadrons thus being liberated. This state of matter, the hot and dense fireball made of liberated quarks and gluons is called as the Quark Gluon Plasma (QGP).

This simple picture has originally provided the basis for models of the quark-hadron transition and has been essentially confirmed by numerical lattice QCD calculations at finite temperature. Figure 1.1 is a sketch of phase diagram. Although the phase boundary between the hadron matter and the QGP is not well known, lattice calculations gave an estimation of the critical temperature T_c and the baryon density needed for the QGP

formation. According to a recent lattice QCD calculation, T_c at 0 baryon density is 170 MeV. However, the systematic uncertainty of the lattice result is not known since it is unattainable using the reweighting method to consider the volume $V \rightarrow \infty$ when calculating the nuclear density going to 0.

The QGP searches have been performed in heavy ion collisions at the Bevatron at Berkeley, the Alternating Gradient Synchrotron (AGS) at BNL, the Super Proton Synchrotron (SPS) at CERN and Relativistic Heavy Ion Collider (RHIC) at Brookhaven National Laboratory. According to the model predictions, RHIC and SPS energy are indeed lying on the phase boundary.

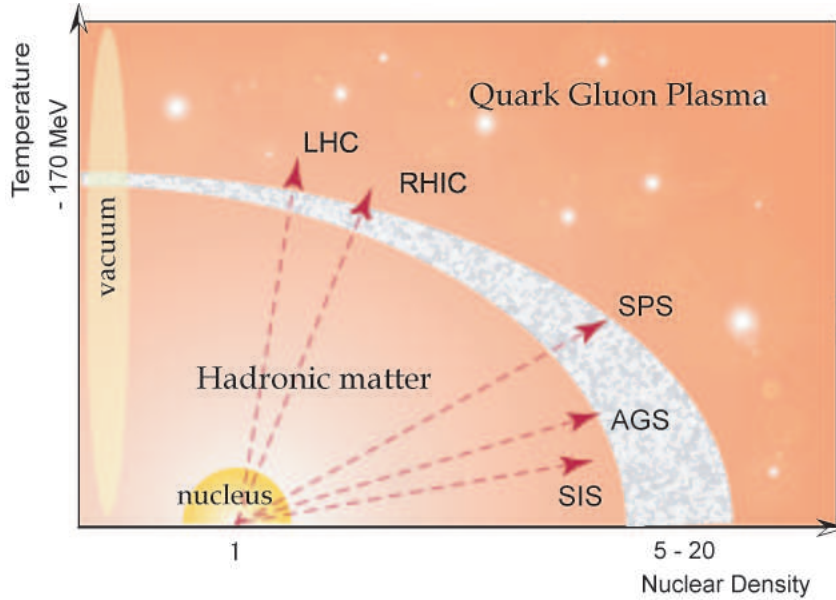


Figure 1.1: Schetch of the QCD phase diagram

1.2 Parton Energy Loss

1.2.1 LPM Effect and Gluon Radiation

The Landau Pomeranchuk Migdal effect[9] is a phenomenon which is introduced in QED. If an electron goes through matter, the LPM effect predicts it loses energy by bremsstrahlung. This phenomenon is confirmed experimentally using high energy electrons and photons [10, 11].

Such interaction between the produced parton with large transeverse momentum and the remnant material is useful probe[12] to study the status of the remnant material. In QCD, a similar effect[17] as LPM effect, which is named as “jet quenching effect”, is

predicted through color bremsstrahlung. When the energetic partons moving through the bulk matter created in the nuclear collision, they lose energy similarly to the way charged particles lose energy through electromagnetic interactions with electrons and nuclei when passing through normal matter. In case of these quarks and gluons going through a QGP, the most important microscopic process is through gluon bremsstrahlung radiation induced by the static gluon fields arranged with a particular (*e.g.* plasma) screening configuration[13]. If energy of radiated gluon is low enough, LPM effect is important. LPM effect occurs when the characteristic formation length ($1/\Delta p$) of the gluon becomes large enough that several gluon scattering centers in the medium can act coherently to interfere in the bremsstrahlung process[14]. A unique feature of QCD bremsstrahlung is other quantum interferences that the radiated gluon interacts with the other gluons making up the color fields and lead to an energy loss. This quantum interference can produce an energy loss $\Delta E/\Delta x$ that grows faster than linearly with the path length L of the parton in the medium [15];

$$\frac{\Delta E}{\Delta x} = \frac{L}{\lambda} \ln \frac{L}{\lambda} \quad (1.5)$$

However, this growth of the energy loss is only valid for a static medium. In a heavy ion collision the rapid decrease of energy density and color charge density in the expanding fireball has to be taken into account.

1.2.2 Parton Energy Loss Models

The most basic initial attempts at modeling the parton energy loss were done with HIJING[16] where simple gluon splitting algorithm were employed to modify the parton fragmentation and effect the energy loss. The early work of Wang and Gyulassy (GW) for incorporating LPM. This idea was expanded upon by many authors. The BDPMS group [14] started by calculating an energy spectrum for emitted gluons $dI/d\omega$ from a single scattering. In this calculation, $dI/d\omega$ is proportional to an effective current J squared. LPM is implemented by summing the products from N scatterings and including a quantum interference term $e^{i\omega}$ for each scattering. This calculation results in an energy loss that is approximately constant ($\propto \log E$) causing a high p_T suppression pattern which diminishes with increasing p_T . This disagrees with suppression behaviors at RHIC in the measured p_T range so far. However, this prediction was not intended to be used in that p_T region.

Currently, the most successful model of high p_T suppression at RHIC energy is the GLV model by Gyulassy, Levai and Vitev. This model employs an operator product formulism which is calculated in a probability amplitudes for gluon emissions. Though the individual single scattering amplitudes are based on the GW model, the amplitudes

are applied in an *opacity expansion* where the number of scattering centers is determined by the *opacity* $\chi = L/\lambda$. L is the length of traversed and λ is the mean free path. The authors found that the expansion can be applied at all orders by a recursive algebraic formula starting from a simple set of lowest order single and double scattering *Born* amplitudes. The lowest term in the opacity expansion is found to be most important because the probability distribution for gluon emissions are folded with an initial density of gluons. This can be translated into dN_g/dy for the scattering centers and has time dependence to account for Bjorken expansion. By the GLV calculation, the energy loss at RHIC energies $\Delta E/\Delta x$ turned out to be nearly constant below jet energy $E = 20$ GeV, which matches the RHIC results showing a p_T independent suppression.

1.2.3 Recent Results

The PHENIX experiment at RHIC has performed a set of measurements of light mesons ($\pi^0, \eta, \phi, J/\psi$ and ω) as shown in Figure 1.2. At intermediate p_T , ϕ meson, which consists of $s\bar{s}$, is less suppressed than π^0 and η . This suggests that quark flavor may be sensitive to energy loss in the medium. Therefore, further investigations are required for understanding the influence of quark flavor composition on the suppression.

In this work, we measure K_S^0 mesons, which includes strangeness quark, in higher p_T region to explore the flavor dependence of the interaction.

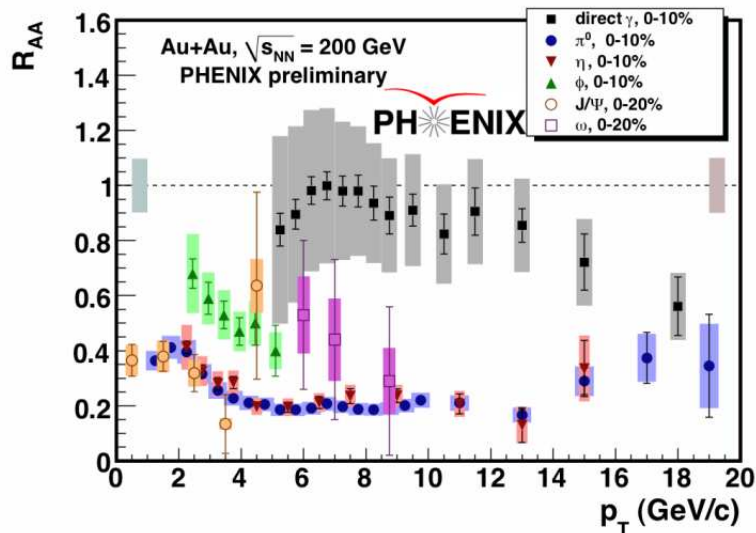


Figure 1.2: Nuclear modification factor R_{AA} of different mesons ($\pi^0, \eta, \phi, \omega, J/\psi$) and direct photons at midrapidity

Chapter 2

Experimental Setup

2.1 RHIC Accelerator

The Relativistic Heavy Ion Collider (RHIC)[22] at Brookhaven National Laboratory provides collisions of various ion; polarized proton, deuteron, Cu and Au. THE RHIC is designed to accelerate protons up to 250 GeV and Au nuclei up to 100 GeV per nucleon.

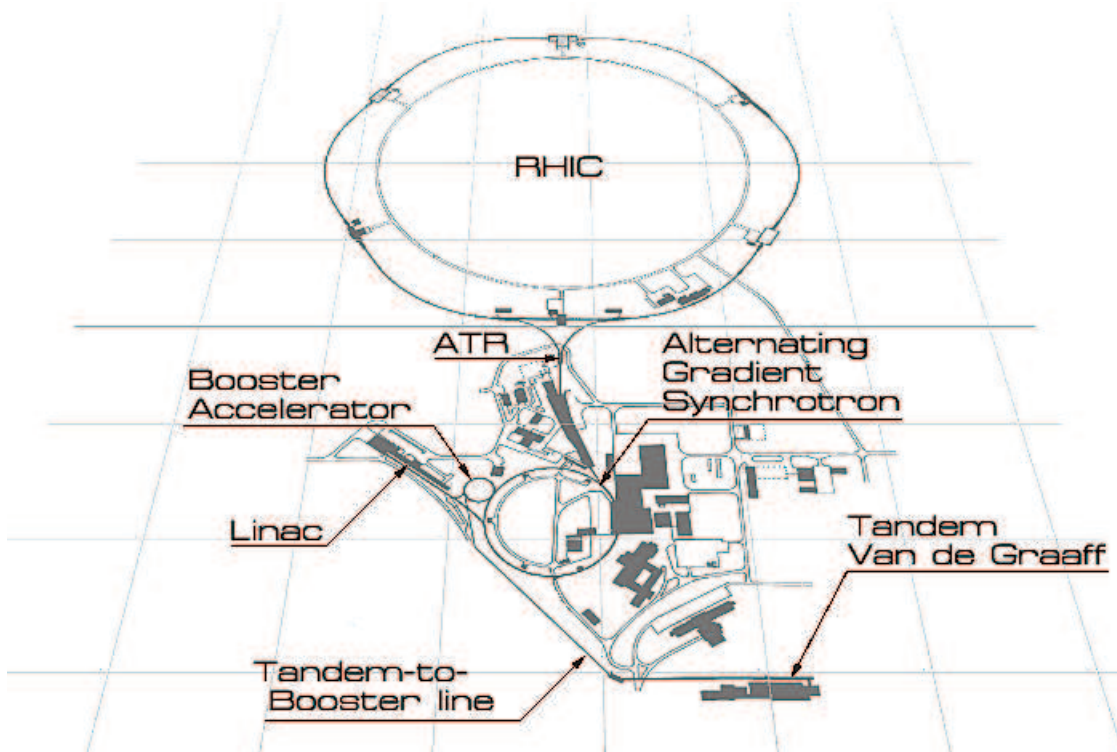


Figure 2.1: Schematic view of the RHIC complex

Figure 2.1 shows a schematic view of the RHIC complex. The Au ion beam starts its journey in the Tandem Van de Graaff and accelerated up to 1 MeV per nucleon. The Tandem Van de Graaff consists of two electrostatic accelerators which is capable of producing voltage up to 15 million volts, and the ions are injected into the Booster. The Booster accelerates them up 95 MeV per nucleon. They are injected into the Alternating Gradient Synchrotron (AGS) and accelerated to 8.86 GeV. When the ion beam reaches top speed in the AGS, they are injected into the next beamline called the AGS-To-RHIC (ATR) transfer line. Once they reach the end of the ATR transfer line, the ions are divided into two bunches, traveling either clockwise or counterclockwise in the so-called *blue* and *yellow* lines. The RHIC main ring has a circumference of 3.8km with the maximum bunch of 120 and the designed luminosity is $2 \times 10^{26} \text{ cm}^{-2}\text{s}^{-2}$ for Au ion.

The ring has six intersection points where its two rings of accelerating magnets cross, allowing the particle beams to collide. Figure 2.2 shows its intersection points. If RHIC's ring is thought of a clock face, the four current experiments are at 6 o'clock (STAR), 8 o'clock (PHENIX), 10 o'clock (PHOBOS) and 2 o'clock (BREMS). There are two additional intersection points at 12 and 4 o'clock where future experiments may be placed. PHENIX, which is the largest of the four experiments where this analysis data is taken. PHENIX is designed specifically to measure direct probes of the collisions such as electrons, muons and photons by its multi purpose detectors. The PHENIX detector and its various detector components are described in the subsequent sections.

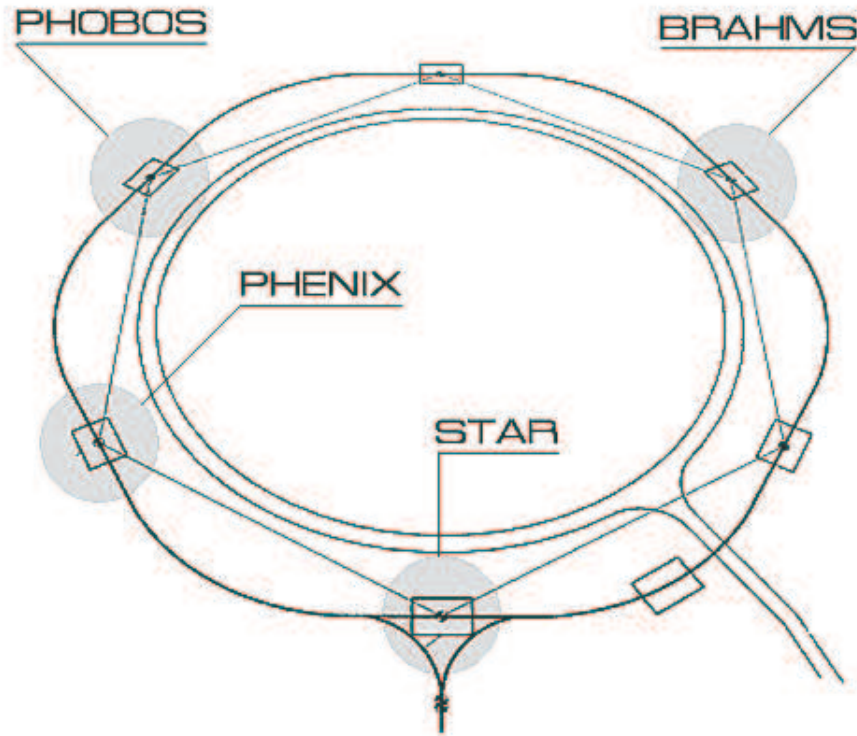


Figure 2.2: RHIC intersection points

2.2 PHENIX Detector

The PHENIX¹ detector at RHIC is designed to perform a broad study of Au+Au, p+p, and p+p collisions to investigate nuclear matter under extreme conditions. In order to carry out this the PHENIX detector utilizes a variety of detector technologies. It uses global detectors to characterize the collisions, a pair of central spectrometers at mid rapidity to measure photons, electrons and hadrons, and a pair of forward spectrometers to measure muons.

¹The Pioneering High Energy Nuclear Interaction eXperiment

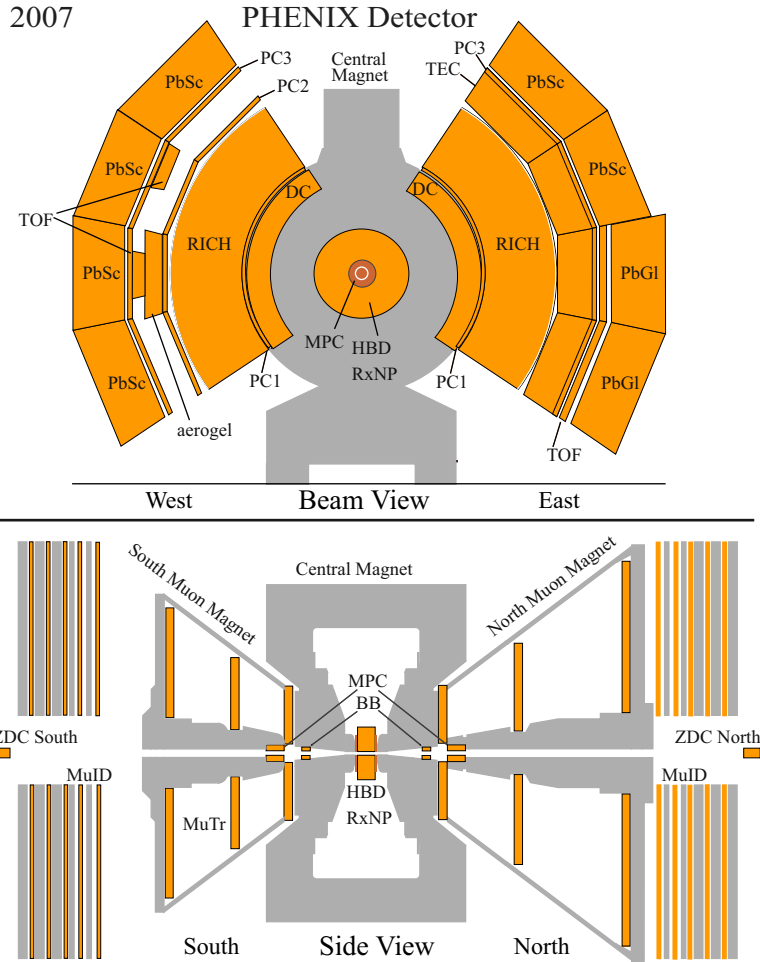


Figure 2.3: Location of the PHENIX subsystems

2.2.1 Global Detectors

In order to characterize nature of a collision, three global detectors are employed. They consists of Beam Beam Counter(BBC), Zero Degree Calorimeter(ZDC) and Multiplicity Vertex Detector(MVD).

Beam Beam Counter(BBC)

Our analysis group contributes to this detector and has a responsibility for it every year.

The Beam Beam Counter(BBC) consists of two identical sets of detectors, each with an array of 64 Cherenkov counters, located 144.35 cm north and south from the nominal collision vertex. The Cherenkov counters are arranged in rings around the beam pipe outside the poles of the central magnet. The BBC detects charged particles in the pseudo-

rapidity region of $3.1 \leq |\eta| \leq 3.9$ and decides whether an inelastic collision occurred.

Furthermore, BBC allows the determination of four important variables; the primary vertex position of the collision, the collision centrality, the start timing for the time-of-flight system, and the reaction plane. Figure 2.4 shows the position of BBC. Using produced particle incoming to the BBC, the z-vertex position(bbc_z) and the collision time(T_0) are calculated as follows;

$$bbc_z = \frac{|T_{north} - T_{south}|}{2} \times c$$

$$T_0 = \frac{T_{north} + T_{south} - 2L/c}{2}$$

where T_{north} and T_{south} are the average hit time with the incoming particles, c is the velocity of light and L is distance between BBC and $z = 0$ point, equals to 144.35cm.

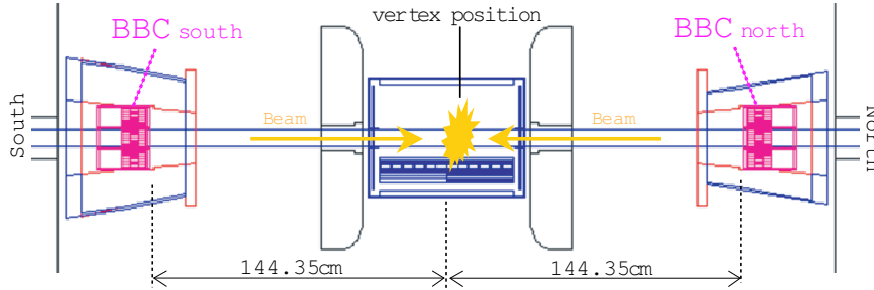


Figure 2.4: The position of BBC

Zero Degree Calorimeter(ZDC)

The Zero Degree Calorimeter(ZDC) is a hadron calorimeter designed to measure the number of neutrons from collision, which are located at 18 m north and south from $z = 0$ position along the beam line. Because both north and south ZDC sit at just the upstream of the last bending magnet of the RHIC ring, most of the charged particles are removed from the ZDC acceptance. Each of them is made of alternating tiles of plates of tungsten and layers of optical fibers. The direction of the plates and layers are tilted by 45° relative to the incident neutron direction to collect the Cherenkov light. This detector provides a common luminosity for all RHIC experiments and common centrality determination. The ZDC is used together with BBC for the measurement of centrality for heavy ion collisions.

2.2.2 Central Spectrometer

The Central Spectrometer is equipped with detectors for measurement of electrons, hadrons and photon. The separation of positive and negative charged tracks are done by applying a magnetic field from the *Central Magnet*.

Magnet System

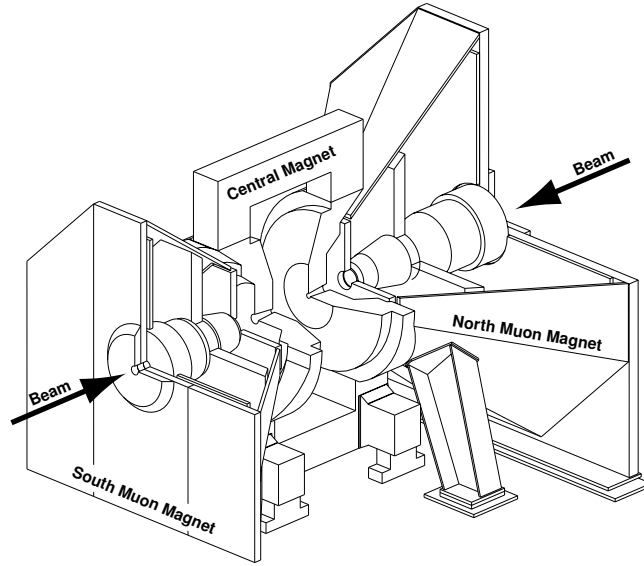
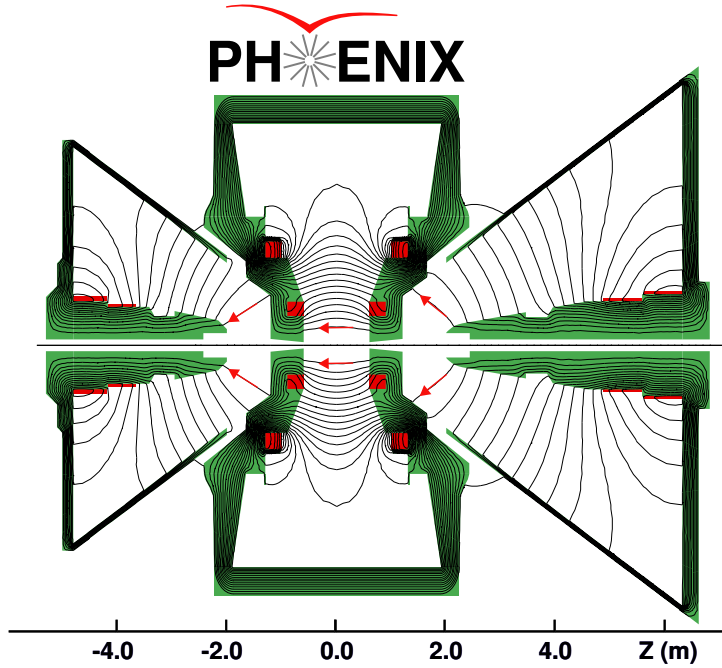


Figure 2.5: Schematic view of the PHENIX magnet system. Arrows indicates the beam direction.

The PHENIX magnet system consists of two magnets with iron yoke and water-cooled copper coils, the Central Magnet (CM) and the North and South Muon Magnet (NMM, SMM). Figure 2.5 shows a schematic view of PHENIX magnet system on a cutaway drawing. The CM provides a magnetic field around the collision point which is parallel to the beam axis. This allows to measure the momentum of charged particles in the polar angle range from 70° to 110° . Figure 2.6 shows lines of the magnetic field. The magnetic field integral varies from 0.43 Tm to 1.15 Tm at $\theta = 90^\circ$.



Magnetic field lines for the two Central Magnet coils in combined (++) mode

Figure 2.6: Megnetic field lines for ++ mode

The MMN and MMS use solenoid coils to provide a radial magnetic field to reconstruct muon momentum. The MMN covers a pseudo-rapidity range of -1.1 to -2.2, and MMS covers a pseudo-rapidity range of 1.1 to 2.4. They cover full azimuthal angle.

Drift Chamber

The Drift Chambers are cylindrically shaped and located in the region from 2 to 2.4 m from the z -axis and 2 m along the beam direction. This places them in a residual magnetic field with a maximum of 0.6 kG. Each DC measures charged particle trajectories in the $r - \phi$ direction to determine transverse momentum p_T of each particle and ultimately, the invariant mass of particle pairs. The DC also participates in the pattern recognition at high particle track densities by providing position information that is used to link tracks through the various PHENIX detector subsystems.

Momentum for a electric charge = 1 paricle is determined with the DC is related to the angle α in mrad by

$$p = \frac{\int_{0.3/R_{DC}} B dl}{\alpha} = \frac{87}{\alpha}$$

where 87 mrad GeV/c is the magnetic field integral.

The DC system consists of two independent gas volumes located in the West and East Arms, respectively. The East Arm detector is the mirror image of the West Arm. Each detector's volume is defined by a cylindrical titanium frame defining the azimuthal and beam axis limits of the detector volume (Fig 2.7).

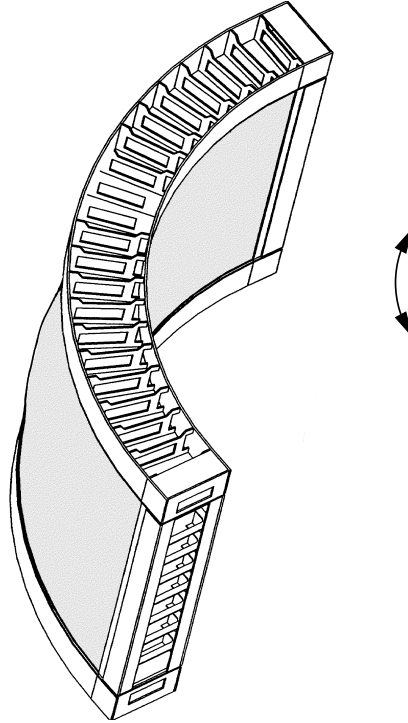


Figure 2.7: Construction of DC frame

Pad Chamber

The Pad Chambers (PC) are multiwire proportional chamber that form three separate layers of the PHENIX central tracking system. Each detector contains a single plane of wires inside a gas volume bounded by two cathode planes. One cathode is finely segmented into an array of pixels. The charge induced on a number of pixels when a charged particle starts an avalanche on an anode wire, is read out through specially designed readout electronics.

The PC system determines space points along the straight line particle trajectories outside the magnetic field. Fig 2.3 shows the location of the PC. The innermost pad chamber plane, called PC1, is located between DC and the Ring Imaging Cherenkov Counter (RICH) on both East and West Arms. PC2 behind the RICH is present in the West Arm only. Also PC3 is mounted just in front of the Electromagnetic Calorimeter

(EMCal) on both arms. The PCs are the only non-projective detectors in the central tracking system and thus are critical elements of the pattern recognition. PC1 is also essential for determining the three-dimensional momentum vector by providing the z coordinate at the exit of the DC.

Time Expansion Chamber

The Time Expansion Chamber (TEC) is composed of a set of 24 large multiwire tracking chambers. The TEC measures all charged particles passing through its active area, providing direction vectors that are matched to additional track information from the DC and PC. The tracking information is used to solve the complex pattern recognition problems associated with the high particle multiplicities in relativistic heavy ion physics. Figure 2.8 shows a schematic operation of the TEC. The anode-cathode configuration is shown together with \vec{E} field lines. A charged track traversing the TEC leaves electron clusters in the gas volume which drift to the anode wires where the multiplication avalanche occurs. This detector allows for systematic studies of tracking efficiency and background rejection versus multiplicity in coordination with the DC. The TEC also enhances the momentum resolution of the Central Spectrometer at $p_T \geq 4$ GeV/c by combining with DC. In addition the TEC measures ionization energy losses (dE/dx) of charged tracks which enables particle identification, particularly electron/pion separation.

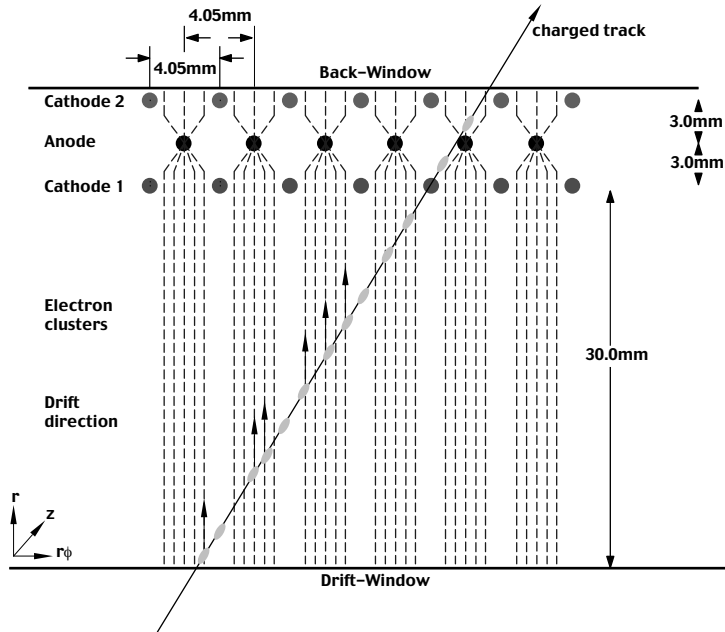


Figure 2.8: Schematic operation of the TEC

Time Of Flight

The Time Of Flight (TOF) system serves as a primary particle identification device for charged hadrons in PHENIX. Its timing resolution is about 100 ps and provides clear separation of π/K up to 2.4 GeV/c and K/p up to 4.0 GeV/c. Figure 2.9 shows a schematic diagram of the components of a single TOF panel. The TOF consists of 10 walls and each contains 96 scintillator slats and photomultiplier tubes which are read out at both ends. The TOF is located at 5.1 m distance from the beam pipe, in between PC3 and the EMCAL in the East Arm.

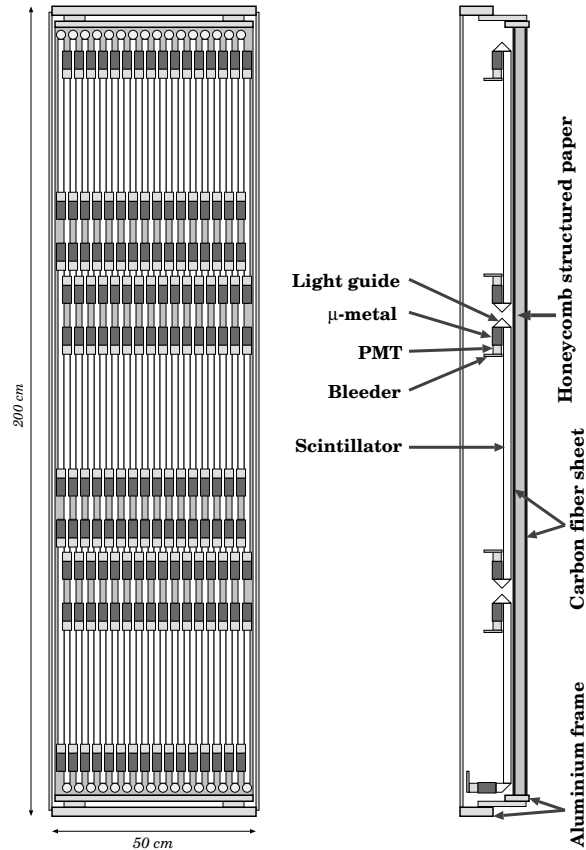


Figure 2.9: Schematic view of the component of a single TOF panel

Ring Imaging Cherenkov

The Ring Imaging Cherenkov (RICH) is designed to identify the electron, positron and high p_T charged particle. Each of the detectors in the East and West Arm has a volume of roughly 40 m³ and minimum thickness of 87 cm of the pressured gas, which is CH₂, N₂, or CO₂ gas depending run periods. During run 2007 for this work, CO₂ gas was

used. RICH provides discrimination of electron/pion below the π^\pm Cherenkov threshold, 4.65 GeV/c. The Cherenkov photons produced in the pressured gas are reflected on the spherical mirror and are detected by the photo multiplier tubes (PMTs). The average size of the Cherenkov ring is 8 cm and the average number of the Cherenkov photons produced by electron is 11 on the plane where the PMTs are sitting. The detector is also used to form a LVL1 trigger in order to enhance the electron, positron and high p_T charged particle. In combination with the EMCal in each arm and the TEC in East Arm, identify e^+ and e^- less than 10^{-4} false.

Aerogel Cherenkov Counter

The Aerogel Cherenkov Counter (AGEL) is the additional particle identifier installed in 2003 since there were some gaps in the particle identification only done by TOF and RICH. This detector provides hadron identification p_T of up to 8 GeV/c. Also, AGEL has an excellent trigger capability for high p_T particles. The AGEL is located between the PC2 and the PC3 in the West Arm. It consists of 160 boxes and each has aerogel with a refractive index of $n = 1.0114$, the best index for a combination with RICH.

Photon Converter

The Photon Converter is placed at about 40 cm distance of the vertex position and is made of brass with 1.7 % radiation length. The purpose is to measure photon yield by tagging electron and positron pair through the pair creation process, $\gamma \rightarrow e^+ + e^-$, and is to study the non-photon source of lepton. By comparing yield of the lepton with and without the Photon Converter, we can separate non-photon and photon source of electron and positron. During run 2007 for this work, the Photon Converter were installed and uninstalled in the middle of the run.

2.2.3 Electro Magnetic Calorimeter

The Electromagnetic Calorimeter (EMCal) plays an important role in detecting photons coming from K_S^0 decay. In this section, the overview of the EMCal system, the detailed specification and the basic performance are described.

Overview of EMCal

In the PHENIX, the electro-magnetic calorimeter (EMCal) is the primary tool for measuring photons, electrons and positrons. In order to cover topics in physics programs, for example a thermal photon measurement in relativistic heavy ion collisions, prompt

	PbSc	PbGl
radiation length (X_0) [mm]	21	29
Moliere radius [mm]	30	37
single channel		
cross section [mm]	52.5×52.5	40×40
depth [mm]	375	400
$[X_0]$	18	14
super-module		
number of channels	144	24
sector		
number of super-modules	18	192
total system		
number of sectors	6	2
number of channels	15552	9216
η coverage	0.7	0.7
ϕ coverage	135°	45°

Table 2.1: Basic parameters of two kinds of PHENIX EMCAL

photon, π^0 and weak boson measurement in polarized proton collisions, the EMCAL needs to cover a wide energy range extending from a few hundred MeV to 80 GeV.

There are two kinds of calorimeter in the PHENIX detector. One is a shashlik type lead-scintillator sampling calorimeter (PbSc) and the other is a lead glass calorimeter (PbGl). Table 2.1 shows their basic parameters. A super-module is composed of 12×12 channels for the PbSc and 4×6 channels for the PbGl. A sector is composed of 18 super-modules for the PbSc and 192 super-modules for the PbGl. The six PbSc sectors and the two PbGl sectors are installed in the outer side of the PHENIX Central Spectrometer. The total EMCAL system in the PHENIX detector consists of the 15552 PbSc channels and the 9216 PbGl channels. The detailed structure of both PbSc and PbGl are described next.

Lead Scintillator Calorimeter

The Lead Scintillator Calorimeter (PbSc) is a shashlik type sampling calorimeter made of alternating tiles of Pb and scintillator covering an area of approximately 48 m^2 . The basic building block is a module consisting of four optically isolated channels which are read out individually. Four channels are mechanically grouped together into a single structural entity called a “module” as shown in the Figure 2.10. The holes with 1.2 mm diameter are placed on both lead and scintillator tiles. The read-out fibers made with wave length

shifter (0.5% POPOP²) pass through the entire channel from one edge to the other edge and return to the first edge after following smooth curves. The both edges of the fibers are gathered into a PMT. The attenuation length of the fiber is approximately 1 m, which affects

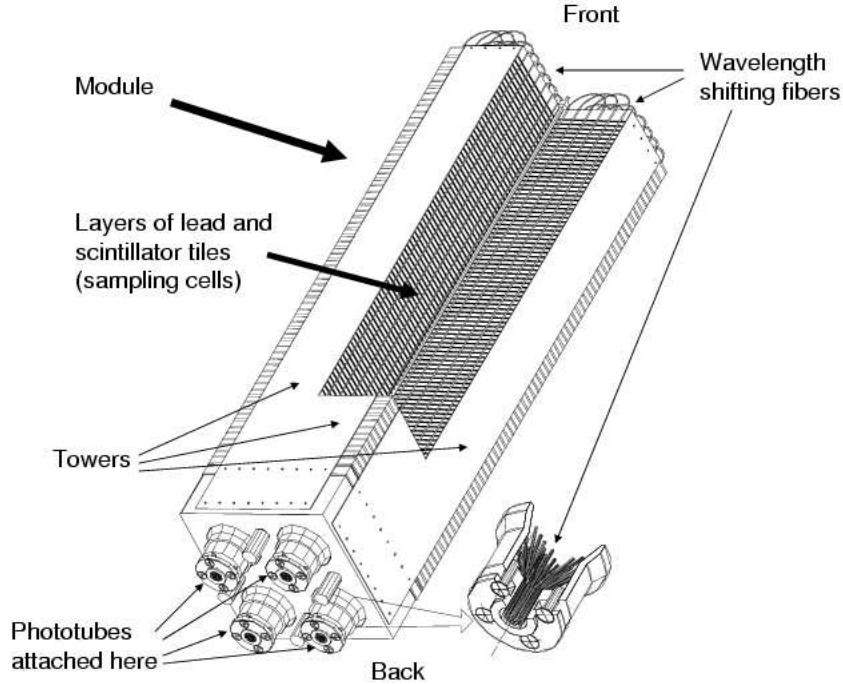


Figure 2.10: Overview of one module of the PbSc EMCAL

The energy resolution of PbSc is

$$\sigma_E/E = 2.1\% \oplus \frac{8.1\%}{\sqrt{E(\text{GeV})}}$$

where \oplus denotes a root of the quadratic sum, $\alpha \oplus \beta = \sqrt{\alpha^2 + \beta^2}$. The angle dependence of the resolution is negligible. This is valid in the energy region of 0.5 GeV to 80 GeV with 1 % systematic uncertainty.

Figure 2.11 shows the measured energy with the PbSc divided by the beam energy as a function of beam energy.

²p-bis[2-(5-Phenyloxazolyl)]-benzene

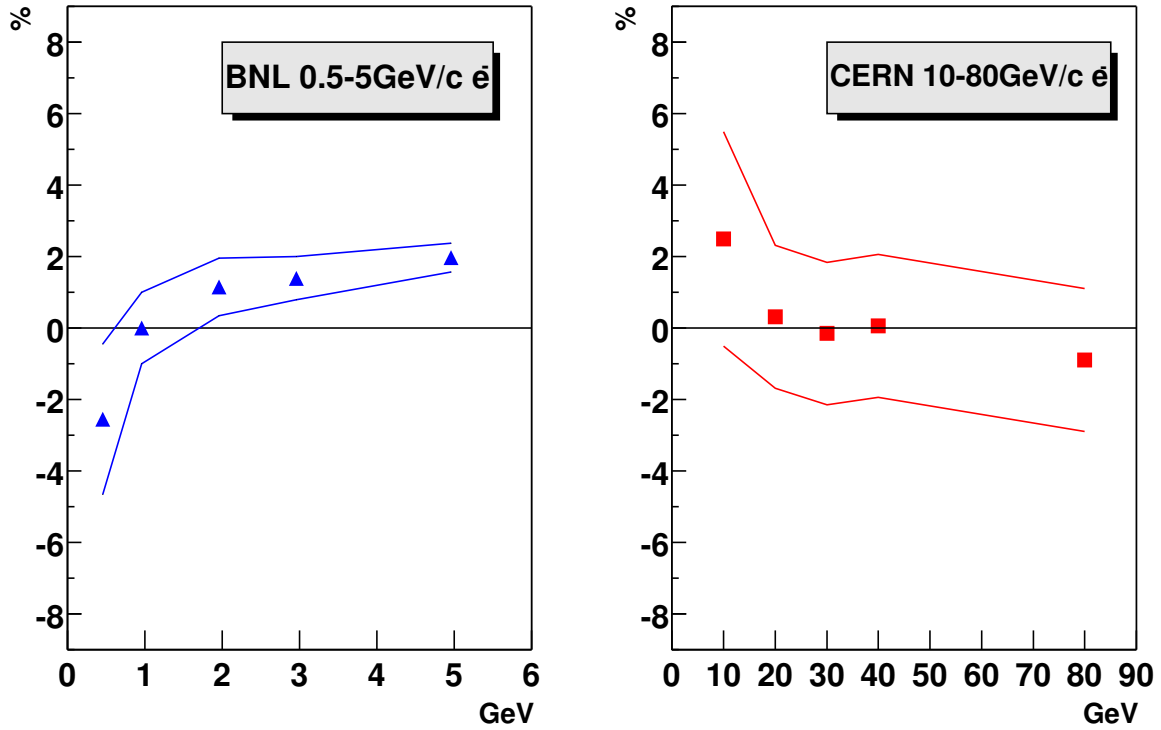


Figure 2.11: Energy linearity by beam tests at BNL (left) and CERN (right). The solid lines show total systematic uncertainties in the analysis

The position resolution of PbSc is

$$\sigma_x(mm) = 1.4(mm) + \frac{5.9(mm)}{\sqrt{E(GeV)}}$$

This is evaluated by beam tests using electron and positron with the well-known impact position on the surface of the EMCal[31].

The timing resolution of PbSc is shown in Figure 2.12.

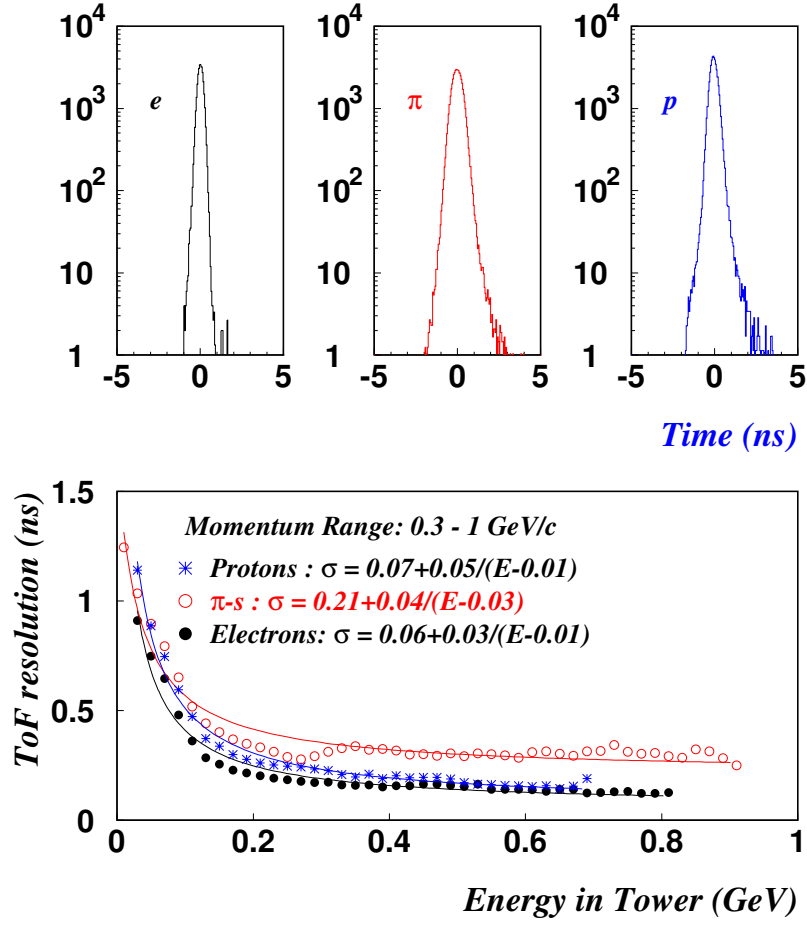


Figure 2.12: PbSc timing resolution for different particles. Top: timing distribution for 1 GeV/c electrons, pions and protons. Bottom: timing resolution in the momentum range of 0.3 - 1.0 GeV/c.

Lead Glass Calorimeter

The Lead Glass Calorimeter (PbGl) is a Cherenkov type calorimeter, which occupies the two lower sectors of the East Arm. Figure 2.13 shows the interior view of one PbGl supermodule, composed by 4×6 channels. The channels within the supermodule are individually wrapped with aluminized mylar foil and shrink tube and are isolated optically. Steel sheets of 0.5 mm thickness are used to house the entire channels and phototubes. The entire array comprises 9216 channels previously used in WA98 experiment at CERN.

The PbGl has a nominal energy resolution as

$$\sigma_E/E = [0.8 \pm 0.1]\% \oplus \frac{5.9 \pm 0.1\%}{\sqrt{E(\text{GeV})}}$$

The measured position resolution is

$$\sigma_x = [0.2 \pm 0.1] \oplus \frac{8.4 \pm 0.3(mm)}{\sqrt{E(GeV)}}$$

Intrinsic timing resolution is better than 300 psec.

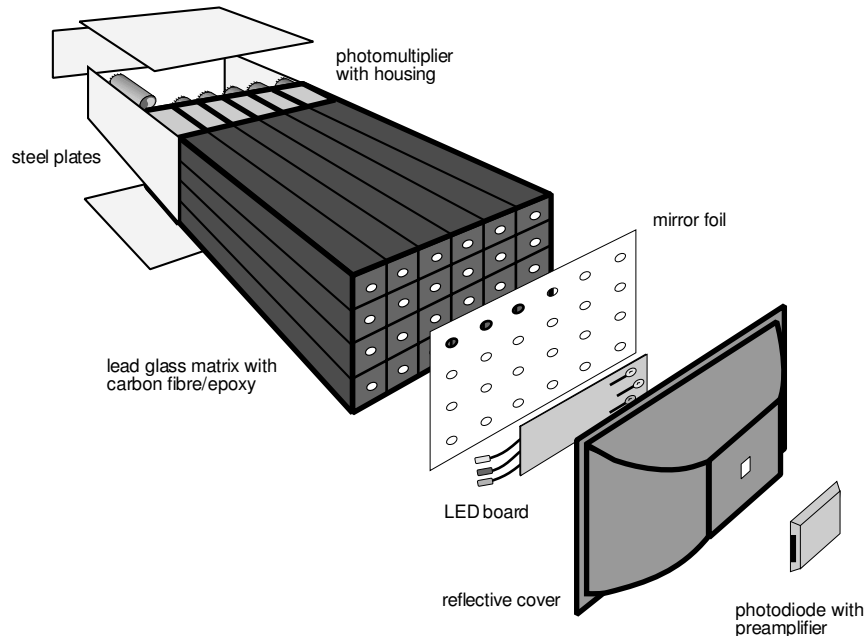


Figure 2.13: Interior view of one PbGl supermodule

2.2.4 Muon Arm Detectors

The Muon Arm is a pair of forward spectrometers which were installed for the purpose of measuring muons. Each muon spectrometer has a large geometrical acceptance and excellent momentum resolution.

Muon Tracker

The Muon Tracker (MuTr) consists of three stations of multi-plane drift chambers that provide precision tracking. Each of three stations of cathode strip chambers presented unique design requirements. All are in the shape of octants built with a 3.175 mm half gap, 5 mm cathode strips and with alternate strips readout. The above design specifications led to the relative mass resolution, approximately given by $\sigma(M)/M = 6\%/\sqrt{M_{\mu\mu}}$, where M is in GeV. This mass resolution enables a clear separation of the ρ, ω peak from the $\phi, J/\psi$ and ψ' .

Muon Identifier

The largest background in the measurement of muon is formed by mis-identified pions and by muons from pion decays. The suppression of such background is achieved by the Muon Identifier (MuID). The MuID consists of alternating layers of steel absorber plates and tracking layers of streamer tubes. The thickness of the plates is decided such that only muons with an energy larger than 2.9 GeV penetrate the MuID completely. The material in front of the MuID, e.g. 30 cm steel backplate of the Muon Magnet, ensures only muons with an energy larger than 1.9 GeV reach the detector. The combination of MuID and absorbers leads to a pion/muon separation of 2×10^{-4} to 3.9×10^{-3} in the momentum region from 2 GeV/c to 10 GeV/c.

2.3 Data Acquisition (DAQ) System

2.3.1 DAQ Overview

The investigation of different colliding system, such as p+p, d+Au, Cu+Cu and Au+Au, requires not only a versatile detector with specialized subsystems but also flexible data acquisition (DAQ) and a triggering system that can handle the high interaction rates, approximately 500 kHz in p+p collisions and a few kHz with large event sizes in Au+Au events.

To cover the broad range of signatures of a possible QGP in heavy ion collisions and to explore the regime of hard scattering at large transverse momenta, it is also necessary to select and enhance rare events via specialized triggers, e.g. on highly energetic photons.

The trigger decisions within the PHENIX experiment are implemented in two different layers, *Level-1* triggers (LVL1) and *Level-2* triggers (LVL2). The fully pipelined LVL1 triggers and the lower levels of the parallel readout are driven by the 9.43 MHz RHIC beam clock³, while the higher levels of the readout and the LVL2 triggers are data-driven, which means that the results are propagated to the next level only after the processing of a given event is completed. The PHENIX DAQ is shown in schematically in Figure 2.14.

³The beam clocks provide a master timing signal that synchronized with the ion bunches in each of the RHIC rings (*Yellow Clock* and *Blue Clock*). And delivered to each experiment. The time of 106 ns for each clock tick accounts for the maximum of 120 bunches in each ring.

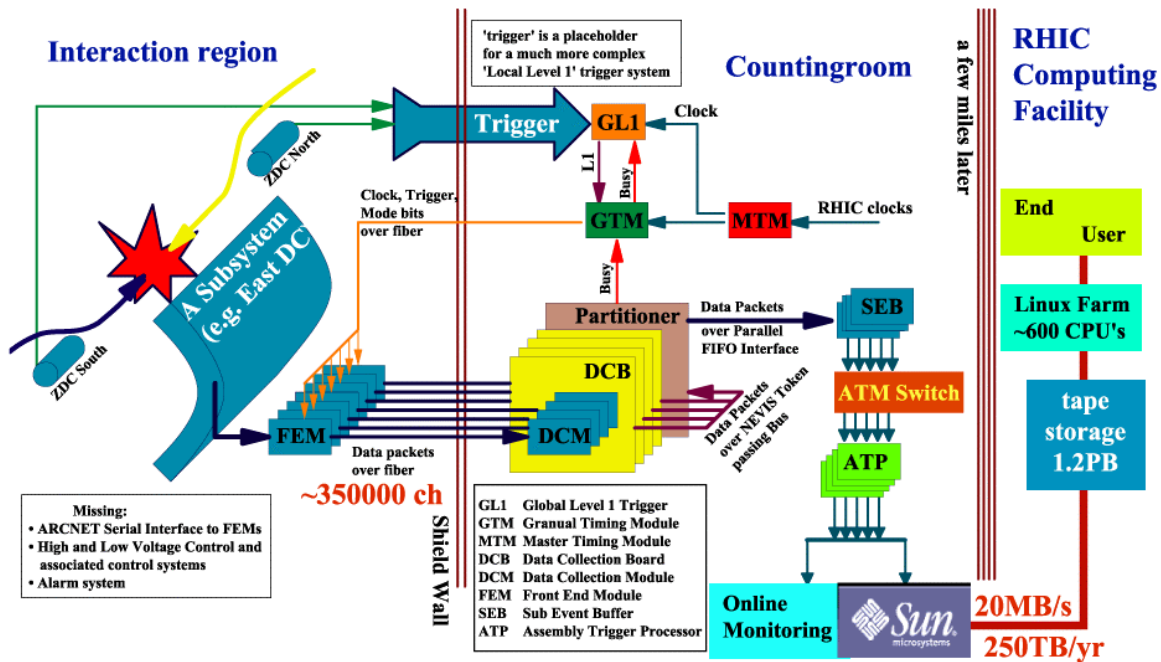


Figure 2.14: Sketch of the PHENIX online system

2.3.2 Front-end Electronics Module

The Front-end Module (FEM) differs in detail for the various subsystems but their general layout is very similar. FEM consists of the Front End Electronics (FEE), which digitize the analog signals from the detector elements and buffer the data to wait for LVL1 trigger decisions. The FEMs also include a Heap Manager (HM), which controls the FEE, formats and communicates to the DCMs, and manages readout requests.

The different subsystems use two approaches to digitize and collect the data. In the first approach, used e.g. for EMCAL, the data are sampled and stored in analog form in switched capacitor arrays called Analog Memory Unit (AMU) and are digitized only after the receipt of the LVL1 accept. The second approach is to digitize the data directly and buffer in Digital Memory Unit (DMU).

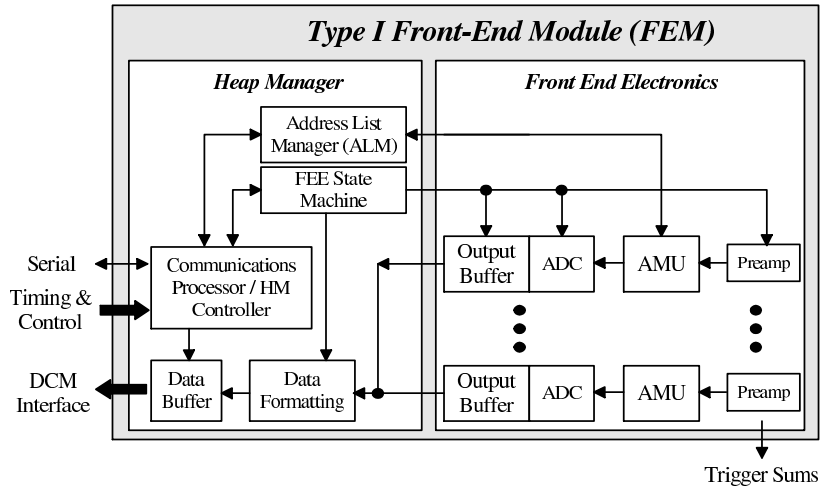


Figure 2.15: Block diagram of Front-end Electronics Module

2.3.3 Data Collection Module

After a LVL1 accept, the data from FEM is transferred via optical fibers from the interaction region to the counting room, where the Data Collection Modules (DCMs) are located (see Figure 2.14). The uncompressed data from about 350,000 channels are formatted, zero suppressed⁴, and checked in parallel in the DCMs. The DCMs also provide buffering for up to five events for output to the Event Builder (EvB) and are able to control the readout of the FEMs via the Granule Timing Module (GTM). The GTM passes the RHIC clock to the different detector combinations (we call such combinations *Granules*) and manages the *busy* and *accept* signals from the trigger.

2.3.4 Event Builder

The main purpose of the Event Builder (EvB) is the final stage of event assembly. It also provides the environment for the LVL2 trigger system. The parallel data streams received from the DCM are transferred to a set of Sub-Event Buffers (SEBs). This modular structure allows easy scalability and maintains the possibility that different collections of detector data streams (*Granules*) can be read out independently. The data in the SEB are checked and transferred on request to the Assembly/Trigger Processor modules (ATPs), where the LVL2 trigger algorithms can decide whether an event is finally assembled from the different data streams and stored on disk for online monitoring and

⁴The ADC values corresponding to no signal are removed from the data stream to allow better compression.

subsequent archiving in tape archives of the RHIC Computing Facility (RCF).

2.3.5 Level-1 Trigger

The task of the LVL1 trigger is to select collision events and to control the rate for the PHENIX DAQ. The Local Level-1 system (LL1) receives parallel input via fibers from different detector subsystems such as BBC, ZDC, MuID, RICH and EMCal. This information is converted into a bit pattern for each RHIC beam crossing and gets summarized by the *Global Level-1 System* (GL1). The GL1 generates a *raw* trigger from the input trigger vectors and checks whether a trigger system or DAQ is busy. If the raw trigger passes this check, it is called *live* trigger. This bit pattern is compared to a scaledown counter and only if this scaled trigger generates an accept, the GL1 initiates the readout of the FEMs via the GTM.

The trigger for an inelastic collision, the minimum bias condition, is given by logical coincidence (& &) of BBC and ZDC. Other LVL1 trigger decisions facilitate the search for rare events e.g. events containing a highly energetic photon, electron, or muon.

2.3.6 Level-2 Trigger

The PHENIX DAQ is capable of handling Au+Au collisions with a rate of approximately 1.4 kHz, corresponds to a data size rate of 224 Mbyte/s. However, archiving the data on disk in the early PHENIX runs was possible only at a rate of 35 Mbyte/s. The necessary reduction of the data volume was achieved by the Level-2 triggers.

The Level-2 trigger system is located in the ATPs and consists of a set of different algorithms, which analyze different detector information and release an event for archiving if a certain trigger condition is satisfied. Unlike the hardware triggers of the LVL1, the software triggers of LVL2 support more complicated operations, e.g. the reconstruction of particle tracks, and thus provide a more precise selection of interesting events.

Chapter 3

Analysis

3.1 Data Set

The data set is Au+Au collisions at center of mass collision energy per nucleon pairs of 200 GeV taken at the PHENIX in 2007. This period is called “Run7”.

3.1.1 Trigger Selection

In this analysis, we used minimum bias events, which are given by logical coincidence (&&) between BBC and ZDC. This trigger accepts 92.2% of the inelastic collisions for Au+Au collisions at $\sqrt{s} = 200$ GeV.

In addition to the trigger selection, we required that the z vertex of a given event lies within the range $-30\text{cm} \leq z \leq 30\text{cm}$, in order to exclude regions that are shadowed by the pole tips of the central magnet and to minimize the background of scattered particles. Figure 3.1 shows the distribution of collision vertex measured by BBC.

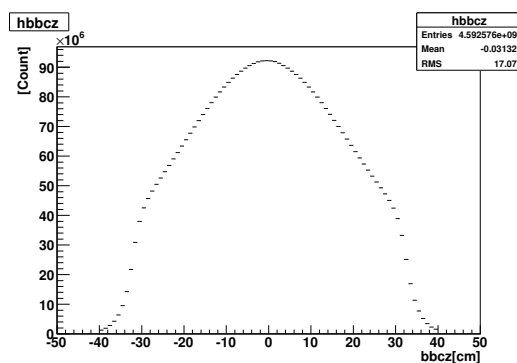


Figure 3.1: Distribution of collision vertex measured by BBC. This distribution is obtained through the online vertex selection by BLL1.

3.1.2 Run by Run Quality Assurance

Before starting the analysis, we removed runs showing a large deviation from the average behavior, e.g. badly calibrated runs. Such run by run quality assurance was done by using π^0 of $p_T \geq 2$ GeV/c. Figure 3.2 shows run by run π^0 invariant mass position and Figure 3.3 shows width of measured π^0 mass.

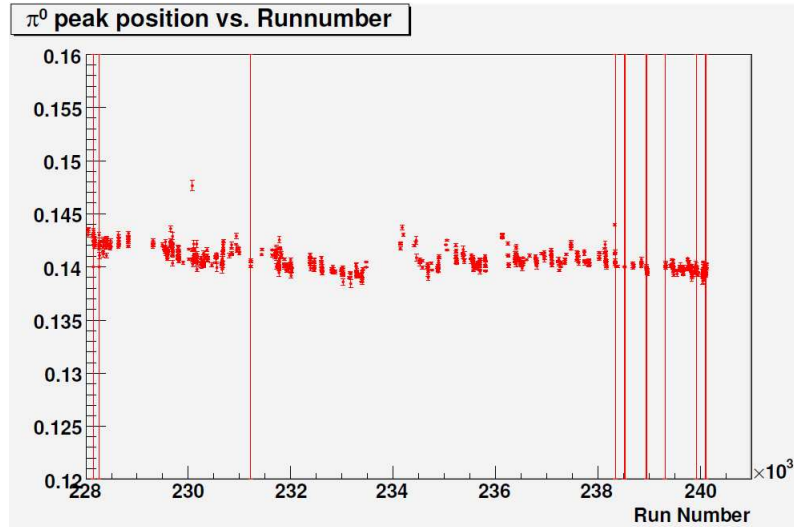


Figure 3.2: Run by run peak positions of π^0 invariant mass

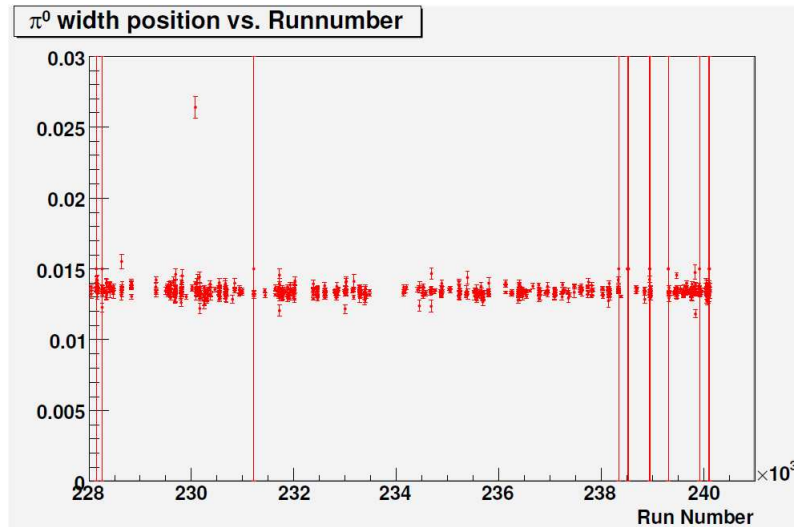


Figure 3.3: Run by run width of π^0 invariant mass

3.2 Centrality Determination

The events, selected by the trigger decisions described above, are analyzed for different impact parameters of the colliding nuclei or centralities to follow the transition from small energy densities and few participants in peripheral events to the hot and dense phase in central collisions.

The centrality for Au+Au collision is determined via the correlation between the number of charged particles passed through the BBC and the energy deposit of neutral particles in the ZDC. The BBC measures the multiplicity of charged particles in the pseudo-rapidity region $3.1 \leq |\eta| \leq 3.9$, while the ZDC detects the energy of neutral particles mostly neutrons as described in Section 2.2.1. With increasing centrality, multiplicity of the detected charge in the BBC increases. The relation between response and centrality is complex. The ZDC is also sensitive to reactions where the nuclei miss each other but neutrons are emitted via the Coulomb interaction¹, such events are excluded by requiring the BBC and ZDC coincidence. Going from peripheral to central events, the excited spectator fragments emit an increasing number of neutrons, which can be detected in the ZDC. If the centrality increases further, most neutrons stay bound, e.g. within deuterons, and are deflected in the magnetic field. In addition, the total number of spectators decreases, leading to less free neutrons that are detected by the ZDC. This behavior is illustrated in Figure 3.5 for the full minimum bias sample. The distribution is divided into the different centralities by an angle ϕ_{cent} in the BBC-ZDC plane defined as:

$$\phi_{cent} = \arctan \left(\frac{(Q_{BBC} - Q_0/Q_{max})}{E_{ZDC}/E_{max}} \right) \quad (3.1)$$

where E_{max} represents the maximum energy of 4,500 GeV deposited in the ZDC and $Q_{max} = 1,700$ the maximum charge-equivalent measured by the BBC. The value of Q_0 , as well as the choice of the angular cuts shown in Figure 3.5, is based on the simulation of the BBC and ZDC signal together with a Glauber model of the Au+Au collision [21]. The cut is chosen in a way that the selected event sample represents a specified fraction of the total geometrical cross section. In this analysis, we consider two parts of centrality, 60-92.2% (peripheral class) and 0-92.2% (minimum bias).

¹In Au+Au collisions at $\sqrt{s_{NN}} = 200$ GeV, approximately 1/3 of all ZDC coincidences are produced by mutual Coulomb excitation of the gold nuclei.

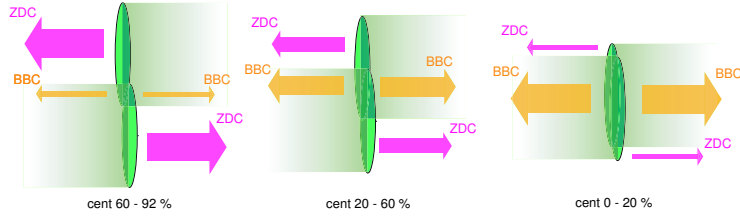


Figure 3.4: Sketch of correlation between signal amount and centrality

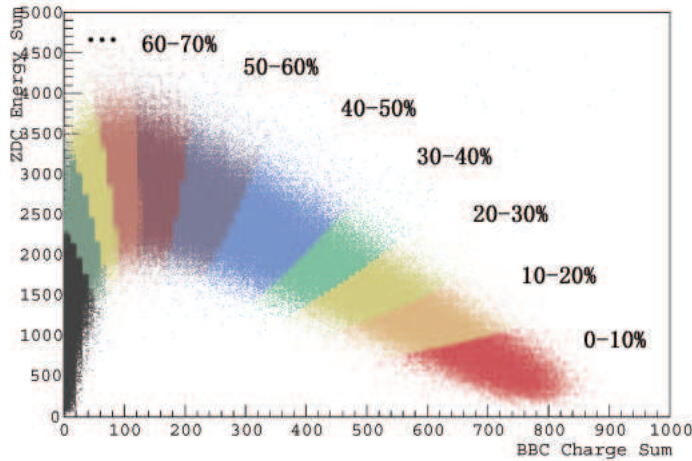


Figure 3.5: Total ZDC signal versus total charge measured by the BBC. Division into different centrality classes is based on this distribution.

3.3 Signal Selection

The main issue of this analysis is the huge combinatorial background for reconstructing. Without signal selection, number of possible combinations is ${}_N C_4 \sim N^4$ and results in no statistical significance of K_S^0 signals. To make it possible to measure K_S^0 mesons in heavy ion collisions, we selected signals by requiring conditions described in this section.

3.3.1 Photon Identification

To facilitate the measurement of photons using the EMCal, certain variables for their identification are computed and associated with the cluster.

Cluster Energy

Clusters of energy < 200 MeV are rejected in the clustering level because the EMCal response at low energy is nonlinear and leads large uncertainty on measured energy. The nonlinearity of EMCal response is described in 2.2.3.

Shower Shape

The main tool to suppress the background from hadrons is a cut on the shower shape because a hadronic shower spreads over wider area than an electromagnetic shower as shown in Figure 3.6. Therefore, the shower shape cut is based on a comparison of the

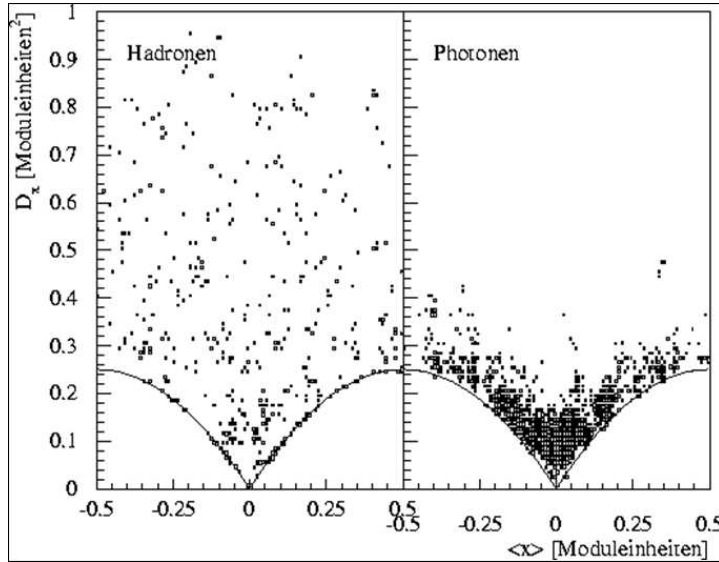


Figure 3.6: Shower shape for hadronic shower (left) and electromagnetic shower (right).

deposited energy in each channel of the measured cluster to the expectation for a cluster formed by an electromagnetic shower of the same energy. The expected energy deposit E_i^{expect} for a given i th channel is determined by a parameterization of the shower shape based on test beams and simulation studies[24, 25]. It depends on (1)the total energy E_{total} of the cluster, (2)the distance to the center of gravity of the shower r , and (3)the angle of incidence θ :

$$\frac{E_i^{expect}}{E_{total}} = p_1(E_{total}, \theta) \cdot \exp\left(\frac{-r^3}{p_2(E_{total}, \theta)}\right) + p_3(E_{total}, \theta) \cdot \exp\left(\frac{-r}{p_4(E_{total}, \theta)}\right) \quad (3.2)$$

Based on this expectation energy for each channel i , we calculate following value:

$$\chi^2 = \frac{1}{N} \sum_{i=1}^N \frac{(E_i^{expect} - E_i^{measured})^2}{\sigma_i^2} \quad (3.3)$$

where N denotes number of channel forming a cluster and $E_i^{measured}$ is the measured energy in channel i . This χ^2 value characterizes how “electromagnetic” a particular shower is. Fig 3.7 shows the χ^2 distributions for 2 GeV/c electrons and pions. In this analysis, clusters with a value of $\chi^2 < 3$ are considered as electromagnetic showers. This cut rejects $\sim 50\%$ of hadronic showers and keeps 98% of photons.

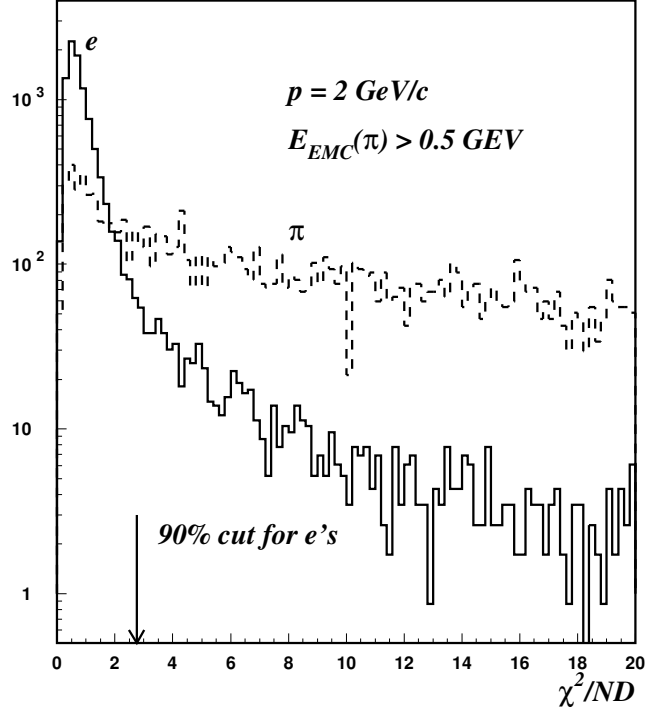


Figure 3.7: χ^2 distribution for showers induced by 2 GeV/c electrons and pions.

Time of Flight

Timing information from the EMCal is used for both photon identification and to find overlapping showers. In particular, timing is the only tool to reject neutral baryons, and anti-neutrons interacting with EMCal are major contributor to clusters with energy $\sim 2 \text{ GeV}/c^2$. Also, large timing difference in different channels forming the same cluster indicates the overlap of two particles with different time of flight. The time of flight from the vertex point to EMCal, TOF_{EMCal} , is computed as follows;

$$\text{TOF}_{EMCal} = (\text{TOF}_{measured} - \text{T0}_{BBC}) - \frac{L}{c} \quad (3.4)$$

where $\text{TOF}_{measured}$ is measured TOF, T0_{BBC} is collision time measured by BBC, L is the distance between the vertex position and EMCal, and c is the velocity of light. Therefore,

EMCal TOF distribution by photon has a peak around 0 nsec, with the resolution ~ 120 ps (See Figure 2.12). Figure 3.8 shows the time of flight distributions for photons and non-photons. Clusters with $|TOF| < 1.5$ ns is used for this analysis.

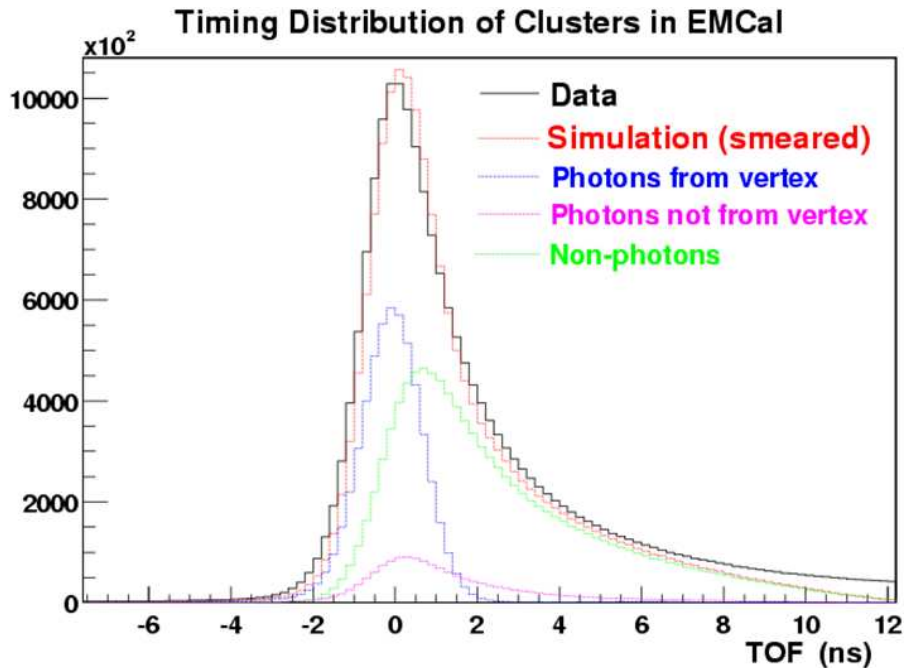


Figure 3.8: Time of flight distributions for photons from vertex and not from vertex, and non-photons obtained by simulation. The black line is obtained by minimum bias event.

Fiducial Area

A cluster, which is formed in the arm edge can leak shower. This makes a measured energy lower. Therefore, clusters lies in two channels from the arm edge are not used in this analysis.

3.3.2 π^0 Identification

Before going to reconstruct K_S^0 , π^0 identification is needed to reduce combinatorial background. π^0 is detected via 2γ decay channel and can be reconstructed by invariant mass of photon pairs. Also, to improve S/N, certain conditions are required on cluster pairs. In this section, we discuss the method of π^0 reconstruction and the criteria for selecting cluster pairs.

Table 3.1: Centrality dependence of π^0 mass position and width. With increasing centrality, econstructed mass shifts higher.

centrality	peak position [GeV/c ²]	width [GeV/c ²]
0-10	0.14256±8.0e-05	0.0125721±1.0e-04
10-20	0.14145±6.0e-05	0.0121617±9.0e-05
20-30	0.14067±5.0e-05	0.0116133±8.0e-05
30-40	0.14000±5.0e-05	0.0112944±7.0e-05
40-50	0.13966±6.0e-05	0.0110868±7.0e-05
50-60	0.13936±7.0e-05	0.0108919±9.0e-05
60-70	0.1391±1.0e-04	0.0110645±1.0e-04
70-80	0.1388±2.0e-04	0.0109653±2.0e-04
80-90	0.1386±4.0e-04	0.0103614±5.0e-04

Invariant Mass Analysis

The invariant mass of a particle pair is given as following;

$$\begin{aligned}
 M_{\gamma\gamma} &= \sqrt{(E_1 + E_2)^2 - (\mathbf{p}_1 + \mathbf{p}_2)^2} \\
 &= \sqrt{2E_1E_2(1 - \cos\theta_{12})}, \tag{3.5}
 \end{aligned}$$

$$\cos\theta_{12} = \frac{x_1x_2 + y_1y_2 + z_1z_2}{\sqrt{x_1^2 + y_1^2 + z_1^2}\sqrt{x_2^2 + y_2^2 + z_2^2}} \tag{3.6}$$

where E_1, E_2 denote cluster energy for γ_1, γ_2 and x_1, x_2, y_1, y_2 are cluster positions in EMCAL. z_1 and z_2 are clusters' z-positions subtracted by z-vertex.

For a photon pair originating from a π^0 pair decay, invariant mass should be identical to the π^0 rest mass of 134.9766 MeV/c². However, due to the finite energy and position resolution in the detection of the photons, the actual reconstructed mass is smeared around a mean value. Also, the reconstructed mass value is influenced by the high multiplicity in a heavy ion collision because overlapping clusters can shift the measured energy of single photon: in central collision events the EMCAL cluster multiplicity is approximately 300, and for peripheral collision events where 80-92.2% centrality the average cluster multiplicity is $\simeq 4.5$.

In order to include those effects, we parameterized peak position and width according to centrality in the first analysis path. Figure 3.9 shows the invariant mass histograms sliced by centrality. To extract mass peak positions and width values, mass spectra are fitted by the function of Gaussian + polynomial. The results can be found in Table 3.1.

Even though a reconstructed mass is equal to the π^0 mass, it can be accidental by background. Therefore, we can't distinguish between π^0 signal and combinatorial background by this method. When reconstructing K_S^0 from 4γ from π^0 pairs, if the mass range

selection is wide, we gain signals from π^0 while combinatorial background increases. On the contrary, if the mass range requirement is narrow, S/N become better though we lose signals. In order to handle such balance and find the best mass window that maximizes S/N, we measured K_S^0 by requiring several π^0 mass ranges independently; peak position $\pm 0.5\sigma, 1\sigma, 1.5\sigma, 2\sigma$, and fixed value $135 \pm 1\sigma$ MeV according to centrality and transverse momentum of K_S^0 .

Energy Asymmetry of Cluster Pair

One possibility to reduce the combinatorial background is to make use of the phase-space distribution of the photons in a $\pi^0 \rightarrow \gamma\gamma$ decay, described as the energy asymmetry;

$$\alpha = \frac{|E_1 - E_2|}{E_1 + E_2} \quad (3.7)$$

where E_1, E_2 is the measured energy of each cluster. $\alpha = 0$ means the two clusters were symmetric energy whereas a $\alpha = 1$ indicates that one of the clusters carried nearly the entire energy of the pair. Since the γ 's are massless and are perfectly symmetric in the center of mass frame under the Lorentz transformation;

$$E_\gamma^{lab} = E_\gamma^{CM} (1 \pm \cos \theta_{CM}) \quad (3.8)$$

Therefore, $|E_1 - E_2| \propto \cos \theta_{CM}$. Since the decay is isotropic the distribution of $\cos \theta_{CM}$ is flat. This is equivalent to a flat distribution of α . On the other hand because of the steeply falling production of photon as a function of energy as shown in Figure 3.11, the vast majority of clusters in EMCal are of low energy. Therefore most combinatorial pairs contain one of those low energy clusters and the α distribution of combinatorial pairs are strongly peaked around 1.

Figure 3.10 shows distributions of α . For the photons originating from π^0 the distribution shows a slight decrease at larger asymmetry region. This is because of the limited acceptance of the EMCal. Decay photons with large asymmetry is equivalent to have a larger opening angle so that one photon can miss the detector.

In this analysis, $\alpha \leq 0.8$ was required for each cluster pair.

Sector Requirement

An angle of decay products from high p_T particle is small due to the Lorentz boost. Therefore, photons from high p_T π^0 decay are detected within near position in EMCal. To reduce combinatorial background, especially at high p_T , we used only cluster pairs that are detected in the same EMCal sector.

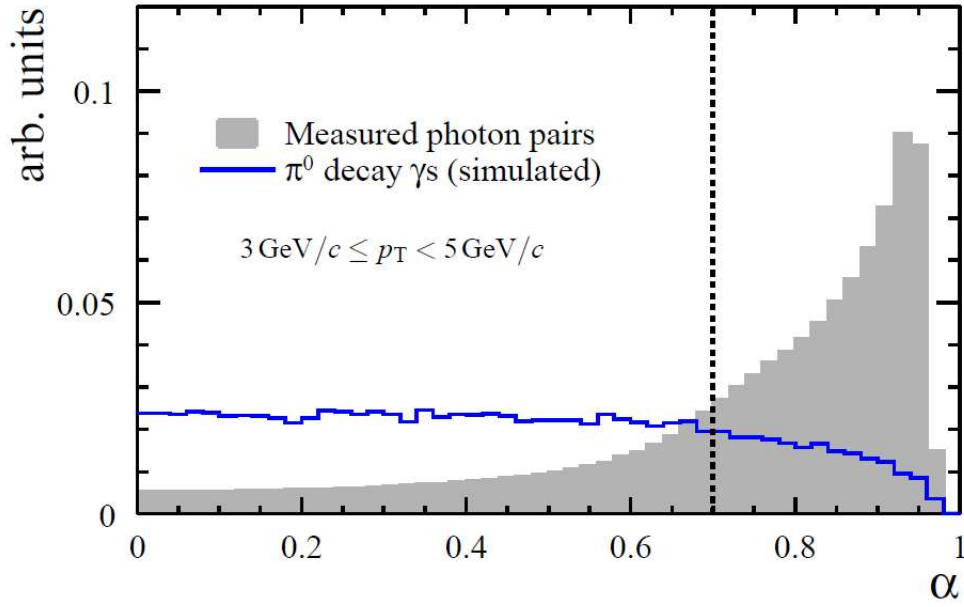


Figure 3.10: Energy asymmetry of photon pairs with $3\text{GeV}/c \leq p_T \leq 5\text{GeV}/c$ from π^0 within the one sector acceptance (simulated) and measured within minimum bias events.

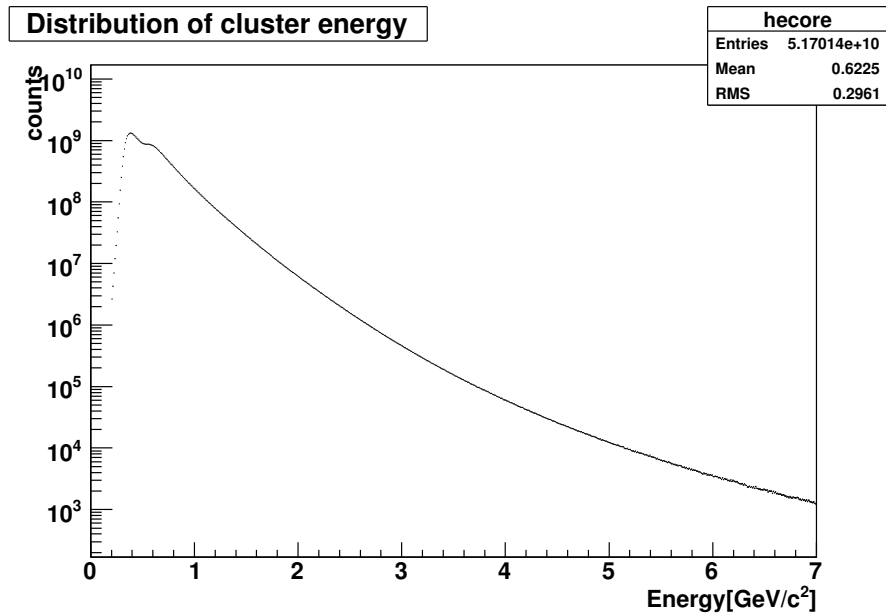


Figure 3.11: Distribution of cluster energy measured in minimum bias events

3.3.3 K_S^0 Identification

K_S^0 mesons are detected via $K_S^0 \rightarrow 2\pi^0 \rightarrow 4\gamma$ decay mode, using clusters passed all requirement described above. In addition to them, we required certain conditions. In this section, we discuss K_S^0 reconstruction and the criteria for selecting π^0 pairs.

Invariant Mass of 4γ

The invariant mass of four photons can be calculated in the same way that used in π^0 reconstruction;

$$M_{4\gamma} = \sqrt{(E_1 + E_2 + E_3 + E_4)^2 - (p_x^2 + p_y^2 + p_z^2)} \quad (3.9)$$

where,

$$\begin{aligned} p_x &= \frac{x_1 E_1}{\sqrt{x_1^2 + y_1^2 + z_1^2}} + \frac{x_2 E_2}{\sqrt{x_2^2 + y_2^2 + z_2^2}} + \frac{x_3 E_3}{\sqrt{x_3^2 + y_3^2 + z_3^2}} + \frac{x_4 E_4}{\sqrt{x_4^2 + y_4^2 + z_4^2}} \\ p_y &= \frac{y_1 E_1}{\sqrt{x_1^2 + y_1^2 + z_1^2}} + \frac{y_2 E_2}{\sqrt{x_2^2 + y_2^2 + z_2^2}} + \frac{y_3 E_3}{\sqrt{x_3^2 + y_3^2 + z_3^2}} + \frac{y_4 E_4}{\sqrt{x_4^2 + y_4^2 + z_4^2}} \\ p_z &= \frac{z_1 E_1}{\sqrt{x_1^2 + y_1^2 + z_1^2}} + \frac{z_2 E_2}{\sqrt{x_2^2 + y_2^2 + z_2^2}} + \frac{z_3 E_3}{\sqrt{x_3^2 + y_3^2 + z_3^2}} + \frac{z_4 E_4}{\sqrt{x_4^2 + y_4^2 + z_4^2}} \end{aligned} \quad (3.10)$$

E_1, E_2, \dots are the measured photon energies and x_1, y_1, z_1, \dots are the cluster positions with reference to the vertex position.

As discussed in 3.3.2, for the four photons originating from K_S^0 this invariant mass are influenced by the cluster overlapping that can shift the cluster energy. Not only such multiplicity effect, but also the long life time of K_S^0 shifts the mass position. As the $K_S^0 \rightarrow \pi^0\pi^0$ is weak decay so the life time of K_S^0 is relatively long; in rest frame, $\tau = 8.953 \times 10^{-9}$ sec and flies $c\tau = 2.68$ cm, which is larger than the position resolution of BBC (e.g. K_S^0 with $p_T = 10$ GeV/c flies $c\tau\beta\gamma = 53.6$ cm). We can't measure a decay position of K_S^0 , therefore we assume that K_S^0 is produced and decayed at a collision vertex. This leads mis-measurement of the vertex point where K_S^0 produced and then makes measured opening angle of decay photons smaller. As invariant mass $M \propto (1 - \cos\theta)$, reconstructed invariant mass is lower than $M = 497.61$ MeV/ c^2 . The amount of mass shift according to centrality and momentum are estimated by simulation study. The details of the simulation is described in 3.4.

Energy Asymmetry of π^0 Pair

As we measure K^0 via $K^0 \rightarrow \pi^0\pi^0$ decay mode, energy asymmetry of π^0 pair can be used for background reduction. Similar to the energy asymmetry of a cluster pair α , energy

asymmetry of π^0 pair is defined as;

$$\begin{aligned}\alpha_{\pi^0\pi^0} &= \frac{|E_{\pi_1^0} - E_{\pi_2^0}|}{E_{\pi_1^0} + E_{\pi_2^0}} \\ &= \frac{|(E_1 + E_2) - (E_3 + E_4)|}{(E_1 + E_2) + (E_3 + E_4)}\end{aligned}\quad (3.11)$$

where E_1, E_2, \dots are measured photon energies.

For the π^0 pairs originating from K_S^0 the distribution steeply decreases around $\alpha_{\pi^0\pi^0} = 1$. This is because the requirement of the same EMCAL sector hit on two photons. $\alpha_{\pi^0\pi^0} = 1$ indicates that one of the π^0 's energy is low. The opening angle of two photons from π^0 is large if π^0 's energy is low, due to the Lorentz boost. The geometrical acceptance for π^0 detection is worse in low p_T as shown in Figure 3.12.

We analyzed applying $\alpha \leq 0.3, 0.4, 0.5, 0.6, 0.8, 0.9$ independently and decided the best value according to centrality and momentum by S/N.

Sector Requirement

For the same reson described in 3.3.2, we required that all four photons are detected in the same EMCAL sector.

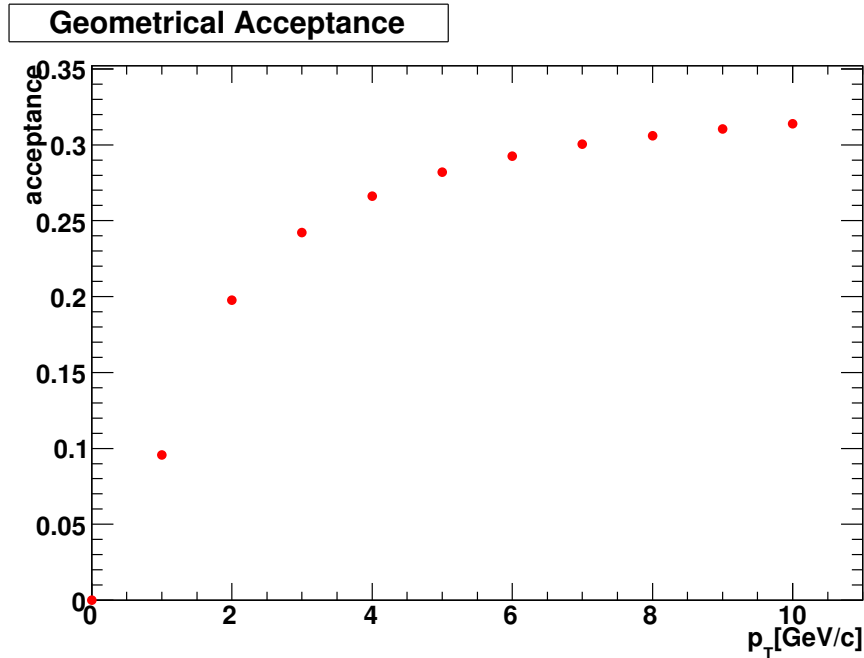


Figure 3.12: Geometrical acceptance for π^0 requiring both photons detected in the same EMCAL sector.

3.3.4 Peak Extraction

To count the number of detected K_S^0 mesons, we fitted the 4γ invariant mass spectra with Gaussian + background shape function defined as follow;

$$f(x) = \left(\frac{1}{500} \frac{A}{\sqrt{2\pi C}} \right) \exp \left[-\frac{1}{2} \left(\frac{x-B}{C} \right)^2 \right] + \exp(D + Ex + Fx^2) \quad (3.12)$$

where A, B, C, D, E, F are free parameters. As the Gaussian integration is;

$$\int_{-\infty}^{\infty} a \exp \left(-\frac{1}{2\sigma^2} x^2 \right) dx = a\sqrt{2\pi\sigma^2} \quad (3.13)$$

so the free parameter A in the fitting function is number of K_S^0 . $1/500$ in the amplitude part is normalization factor because bin width of mass spectra is $1/500 \text{ GeV}/c^2$.

The free parameter B indicates the mean value of reconstructed invariant mass from K_S^0 . As discussed in 3.3.3, mass position shifts due to the cluster overlapping and long life time. Figure 3.13 shows the centrality and momentum dependence of the reconstructed K_S^0 mass which is obtained from embedding simulation. In the fitting, the range of the free parameter B is limited within simulated mass position \pm error.

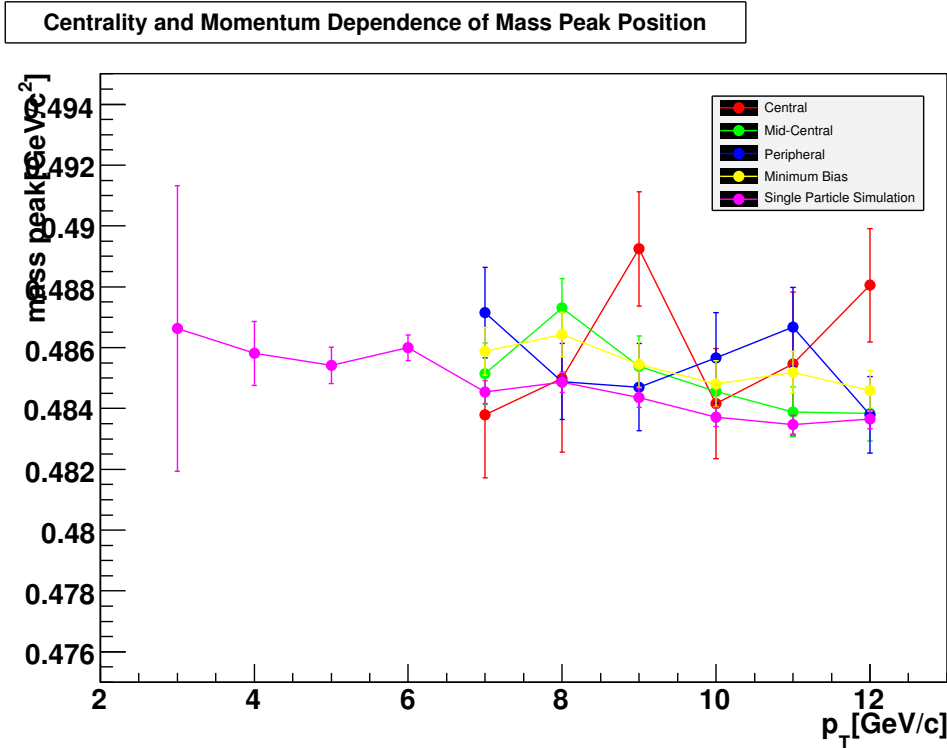


Figure 3.13: centrality and momentum dependence of mass peak position

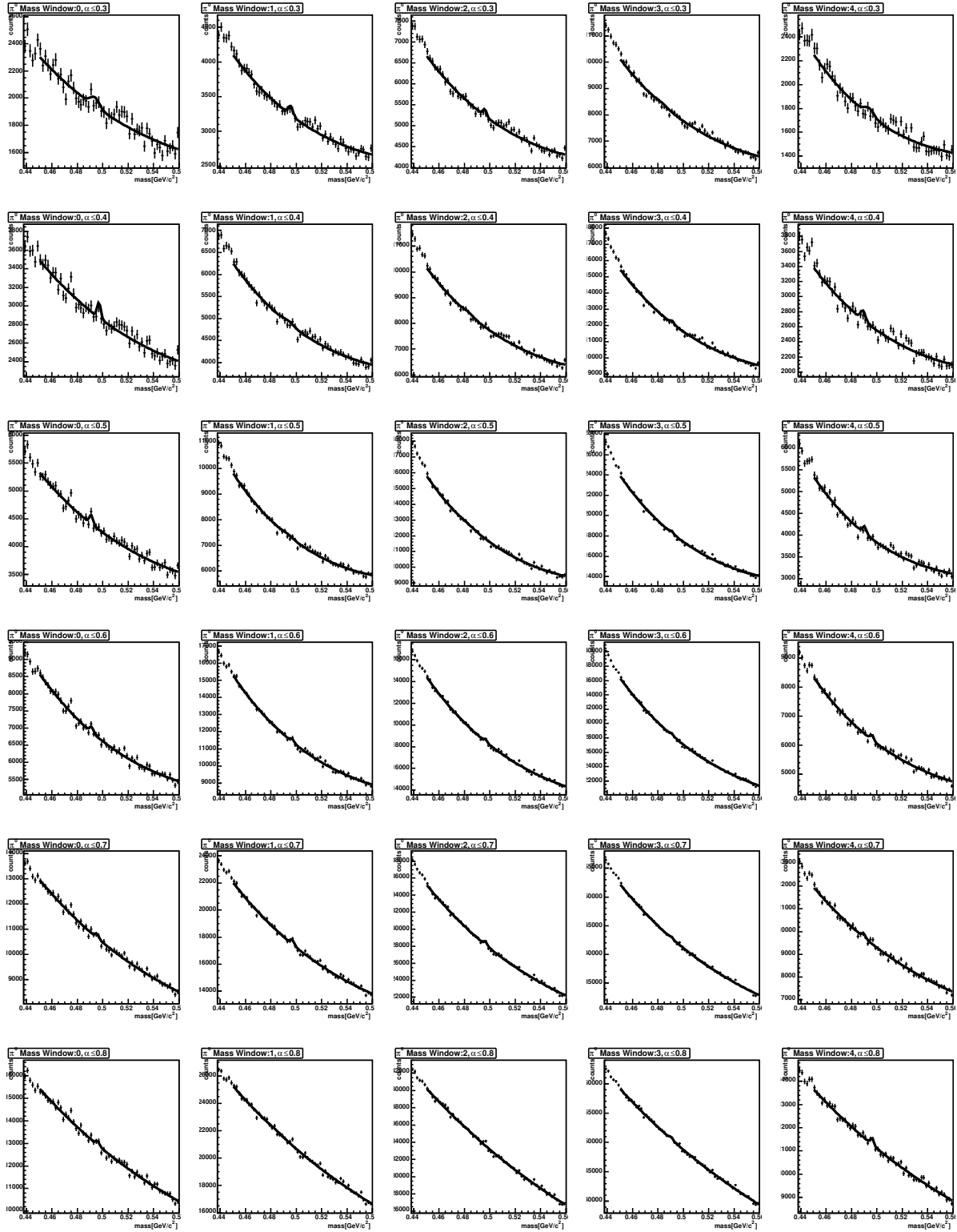


Figure 3.14: Invariant mass spectra for $5.5 \leq p_T < 6.5$ GeV/c, minimum bias event

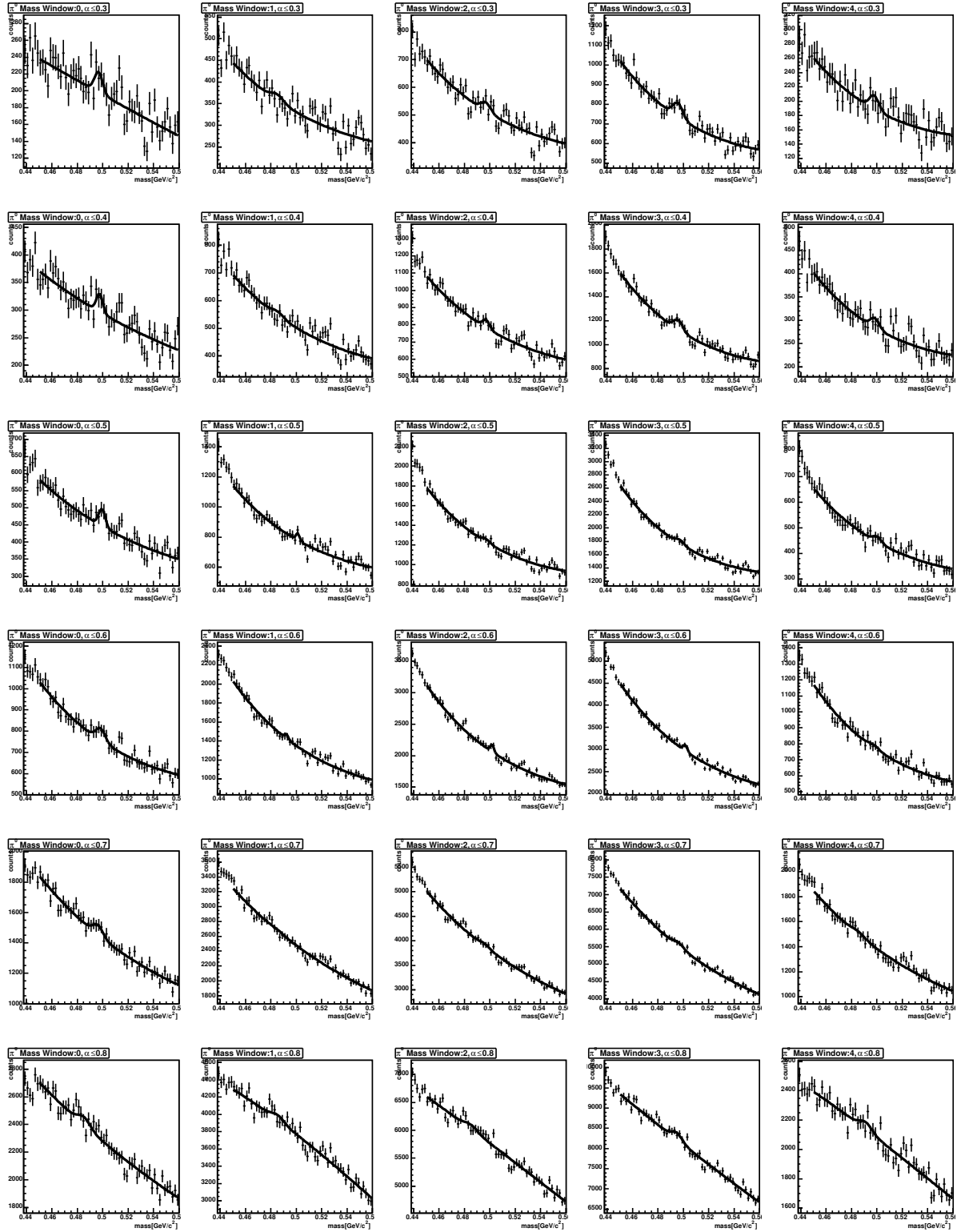


Figure 3.15: Invariant mass spectra for $6.5 \leq p_T < 7.5$ GeV/c, minimum bias event

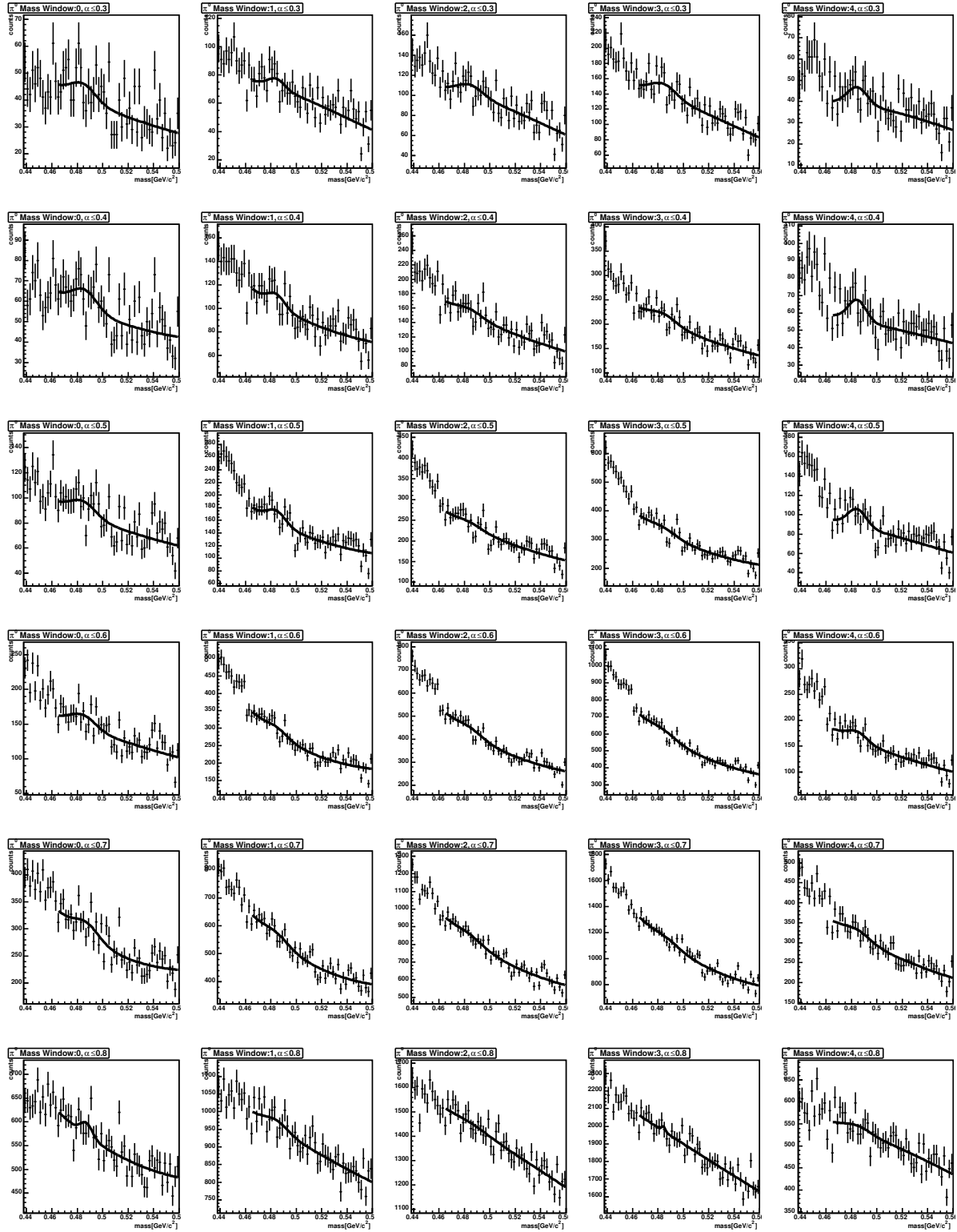


Figure 3.16: Invariant mass spectra for $7.5 \leq p_T < 8.5$ GeV/c, minimum bias event

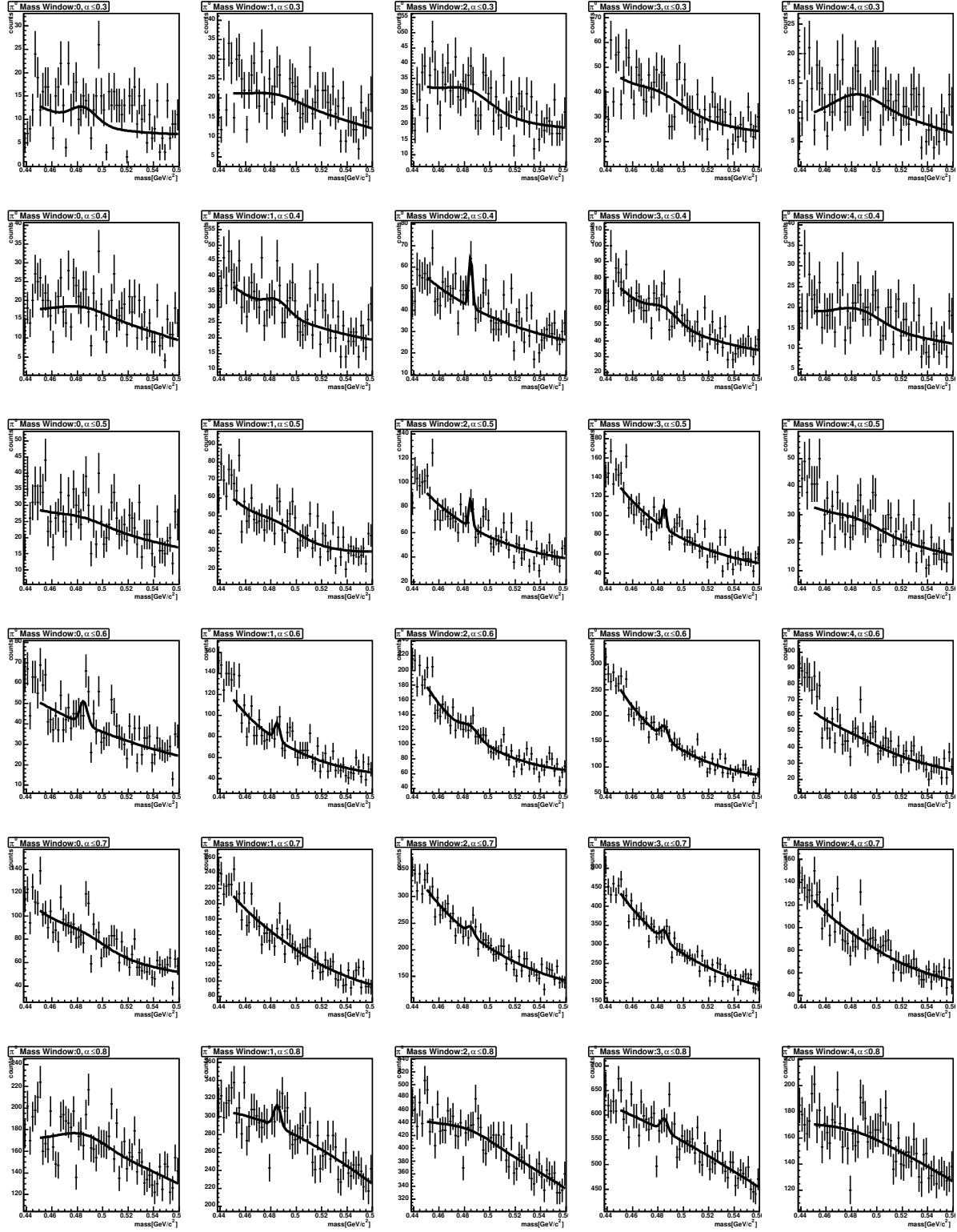


Figure 3.17: Invariant mass spectra for $8.5 \leq p_T < 9.5$ GeV/c, minimum bias event

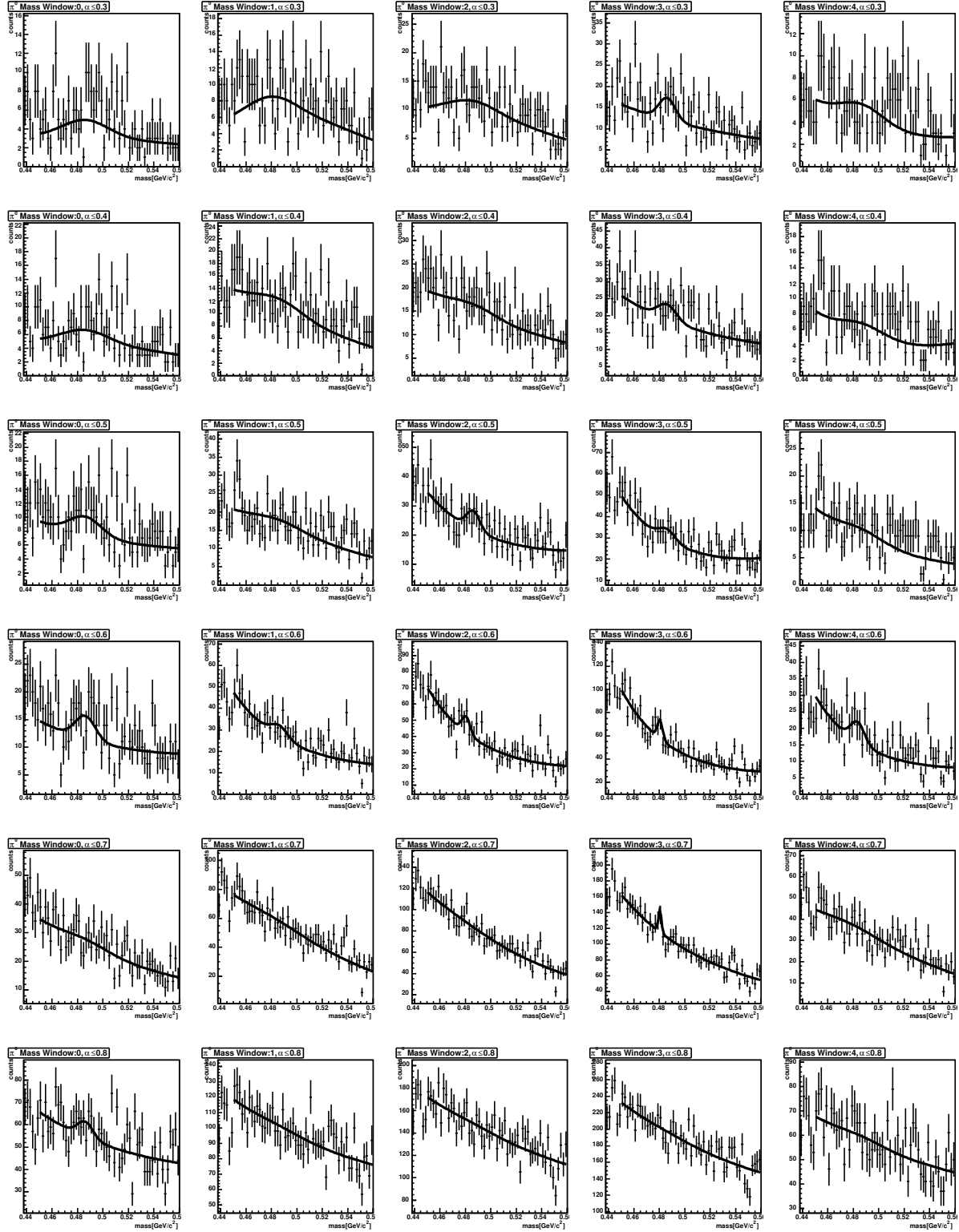


Figure 3.18: Invariant mass spectra for $9.5 \leq p_T < 10.5$ GeV/c, minimum bias event

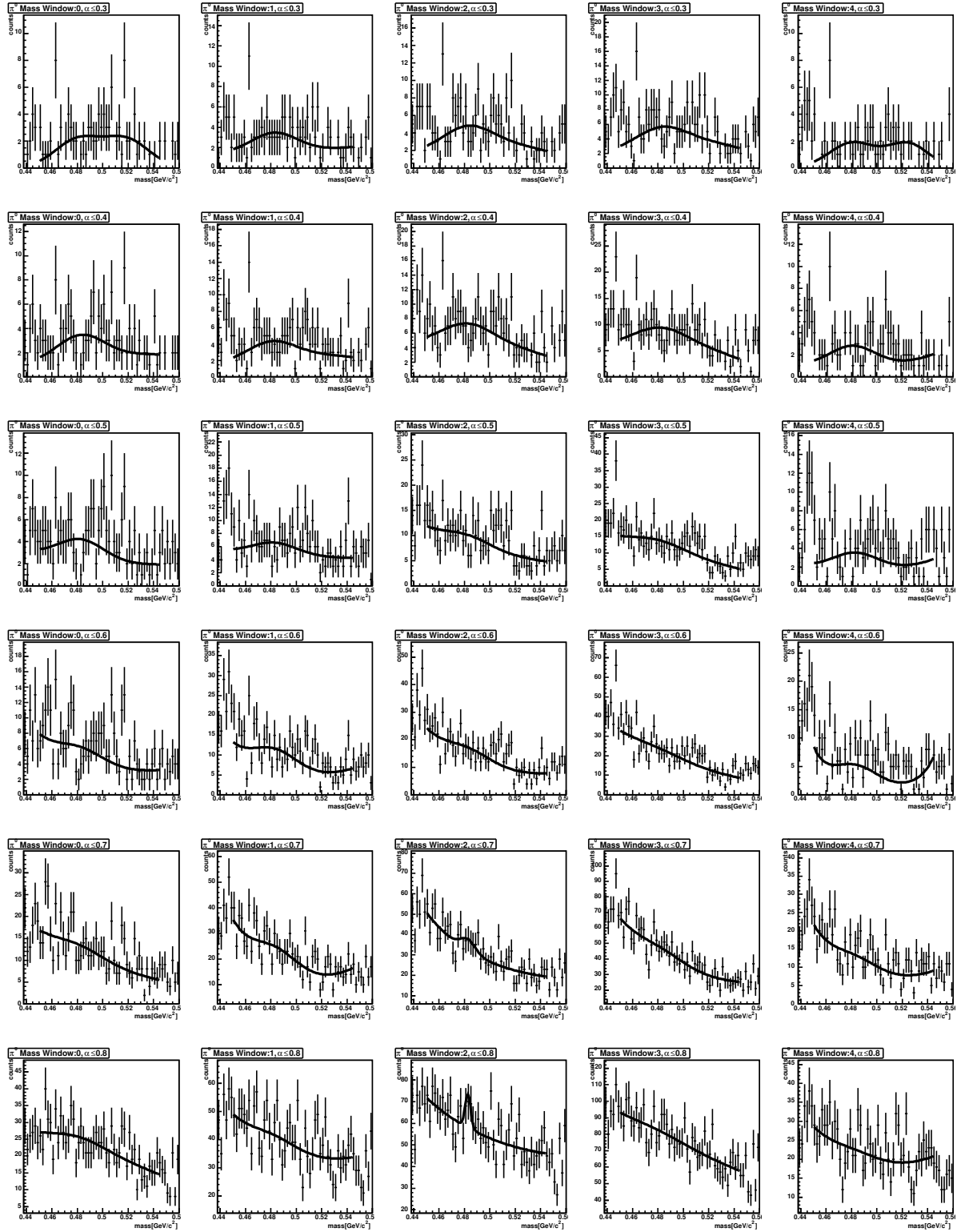


Figure 3.19: Invariant mass spectra for $10.5 \leq p_T < 11.5$ GeV/c, minimum bias event

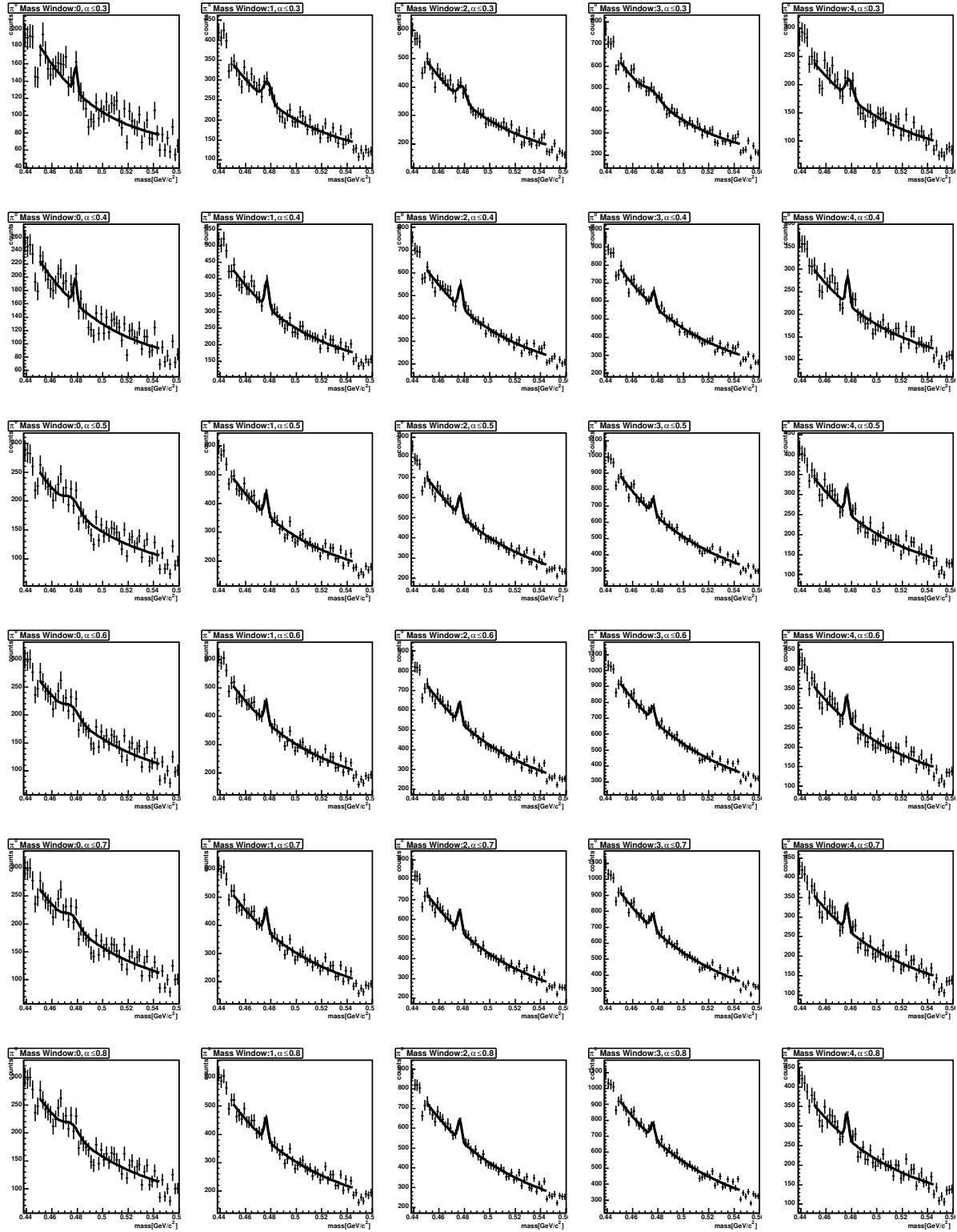


Figure 3.20: Invariant mass spectra for $2.5 \leq p_T < 3.5$ GeV/c, centrality 60-92.2%

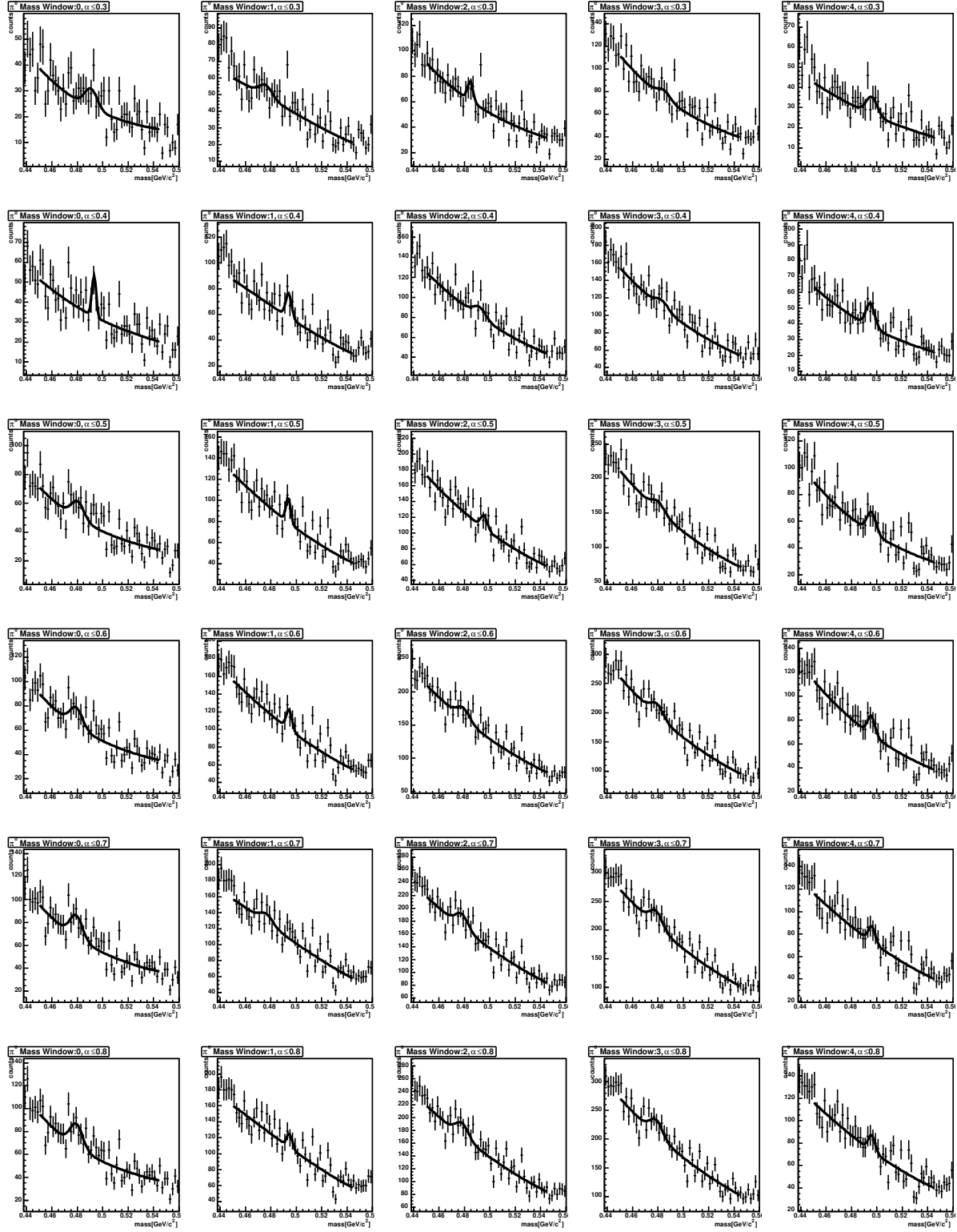


Figure 3.21: Invariant mass spectra for $3.5 \leq p_T < 4.5$ GeV/c, centrality 60-92.2%

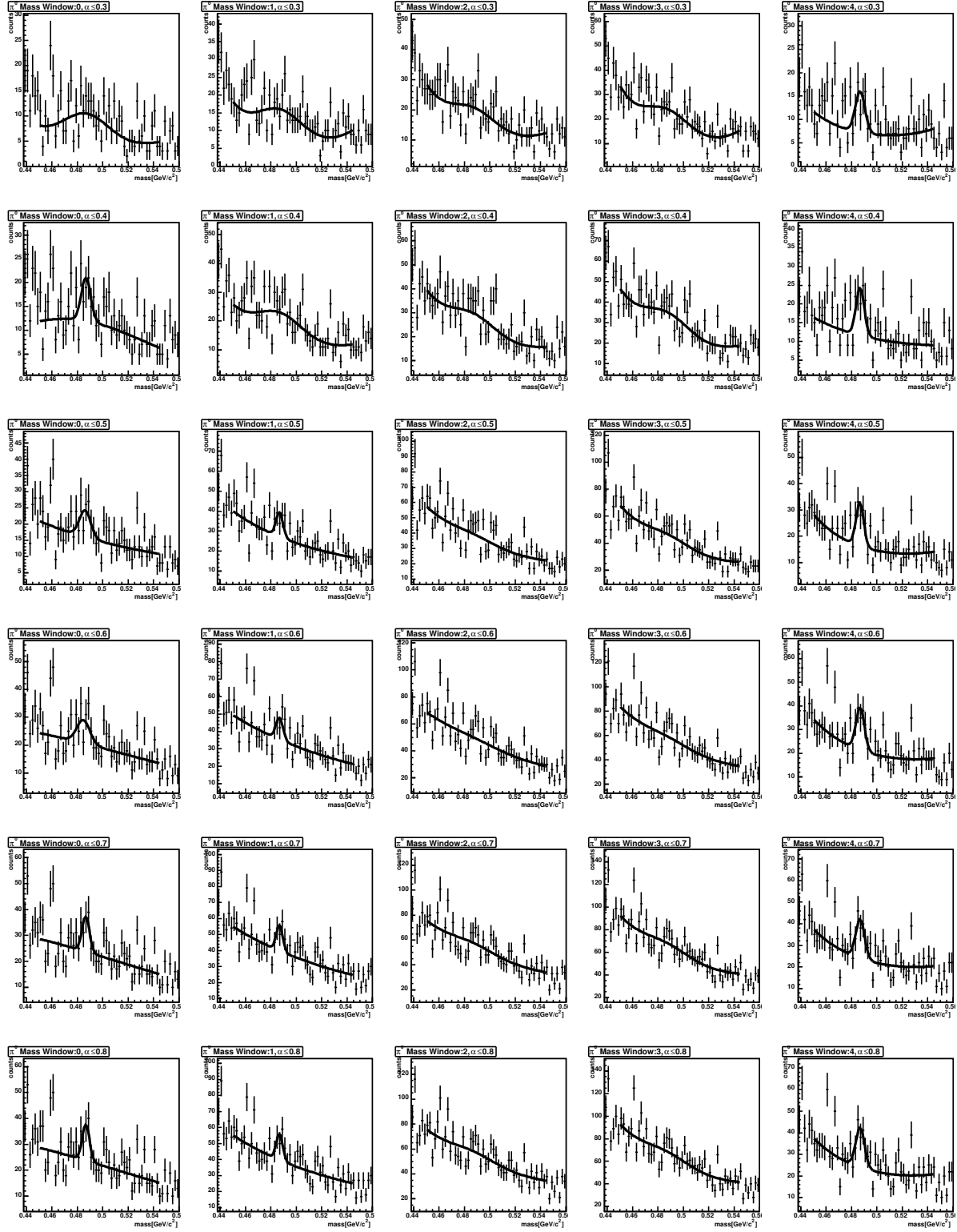


Figure 3.22: Invariant mass spectra for $5.5 \leq p_T < 5.5 \text{ GeV}/c$, centrality 60-92.2%

3.4 Simulation

The extraction of K_S^0 signal, resulting raw count, is still not yet the true physics quantity since its absolute value is still depends on detector geometry, response and resolution. Therefore, estimation of detection efficiency is needed to calculate p_T spectra or invariant yield. In addition, in order to reduce the systematic error for the peak extraction described in 3.3.3, evaluating the shift amount of reconstructed K_S^0 mass and its width is important.

In the simulation, we know the “true” information, number of K_S^0 mesons we input, say $N_{K_S^0}^{input}(p_T)$, and if we extract the raw counts in exactly the same manner (i.e. applying all the same selection criteria on signals) we can calculate detection efficiency ϵ_{detect} with the following formula;

$$\epsilon(p_T) = \frac{N_{K_S^0}^{reconstructed}(p_T)}{N_{K_S^0}^{input}(p_T)} \quad (3.14)$$

where $N_{K_S^0}^{reconstructed}$ is the raw counts extracted in the simulation with the same signal selection criteria as real data analysis.

The single particle generation, which decide p_T , initial ϕ angle and rapidity, is done by the event generator EXODUS. And the simulation of detector response including resolution is carried out using PISA framework.

3.4.1 Event Generator

The input single particles are generated with the following characteristics using the event generator EXODUS which is based on Monte Carlo codes.

- p_T range : 0-15 GeV, with a flat distribution
- pseudo-rapidity : $-0.5 \leq y \leq 0.5$, with a flat distribution
- ϕ angle : $0 \leq \phi \leq 2\pi$, with an isotropical distribution
- z vertex : $-30cm \leq z \leq 30cm$, with a flat distribution

3.4.2 Detector Simulation

PISA² is a simulation application of the complete PHENIX setup based on the GEANT package. GEANT is a program in which a detector geometry can be specified as input, including its materials, to arbitrary precision, along with particle trajectories starting from

²PISA stands for PHENIX Integrated Simulation Application

arbitrary positions. Once these are specified, GEANT will follow the particle, and recursively follow the products of interactions with the specified matter configuration. This allows to make a nearly perfect simulation under a nearly perfect tuning. In PISA, physical process such as annihilation, bremsstrahlung, Compton scattering, multiple scattering and pair production are enabled to simulate.

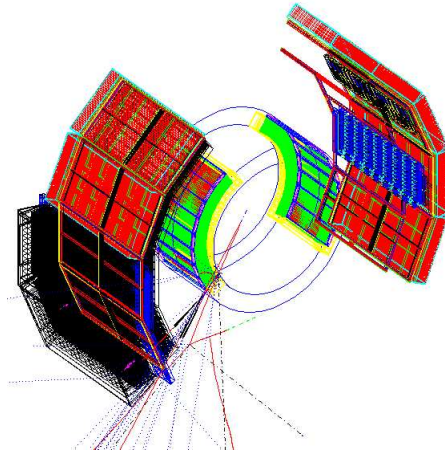


Figure 3.23: An event display of $K_S^0 \rightarrow \pi^+ \pi^-$ decay. This decay is processed in PISA.

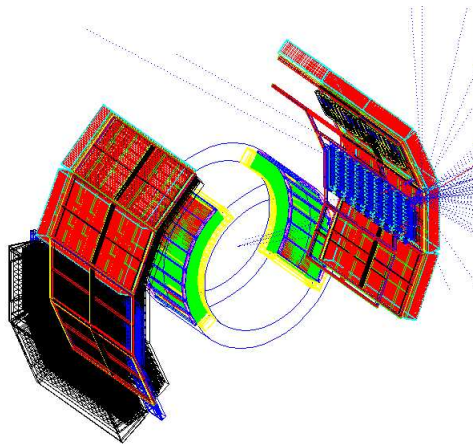


Figure 3.24: An event display of $K_S^0 \rightarrow 2\pi^0 \rightarrow 4\gamma$ decay. This decay is processed in PISA.

3.4.3 Multiplicity Effect Simulation

To evaluate how the measured spectrum is influenced by the high multiplicity environment, we carried out the *embedding* simulation. The general idea of this method is to merge the EMCal data from real events with the data from the simulation of single particle. The main advantage of this technique is that the merged event can be processed within the same clustering algorithm and analyzed within the same framework as the real data. The main flow of the embedding program as shown in Figure 3.25 is described in the following.

Real events are only considered if they satisfy the minimum bias trigger condition and the same vertex cut used during the analysis. The simulated events are scanned prior to the embedding, and their position is sorted into one of twelve vertex classes, each 5 cm wide. This allows to select directly a simulated event with the appropriate vertex for combination with the real event.

For each selected real event the channel information is extracted from the data and merged with the channel data from one simulated event. The merging basically involves the addition of the energies as illustrated in Figure 3.25. In addition to the merged data, information from the simulation (e.g. primary momentum of simulated particle) is added on the output level.

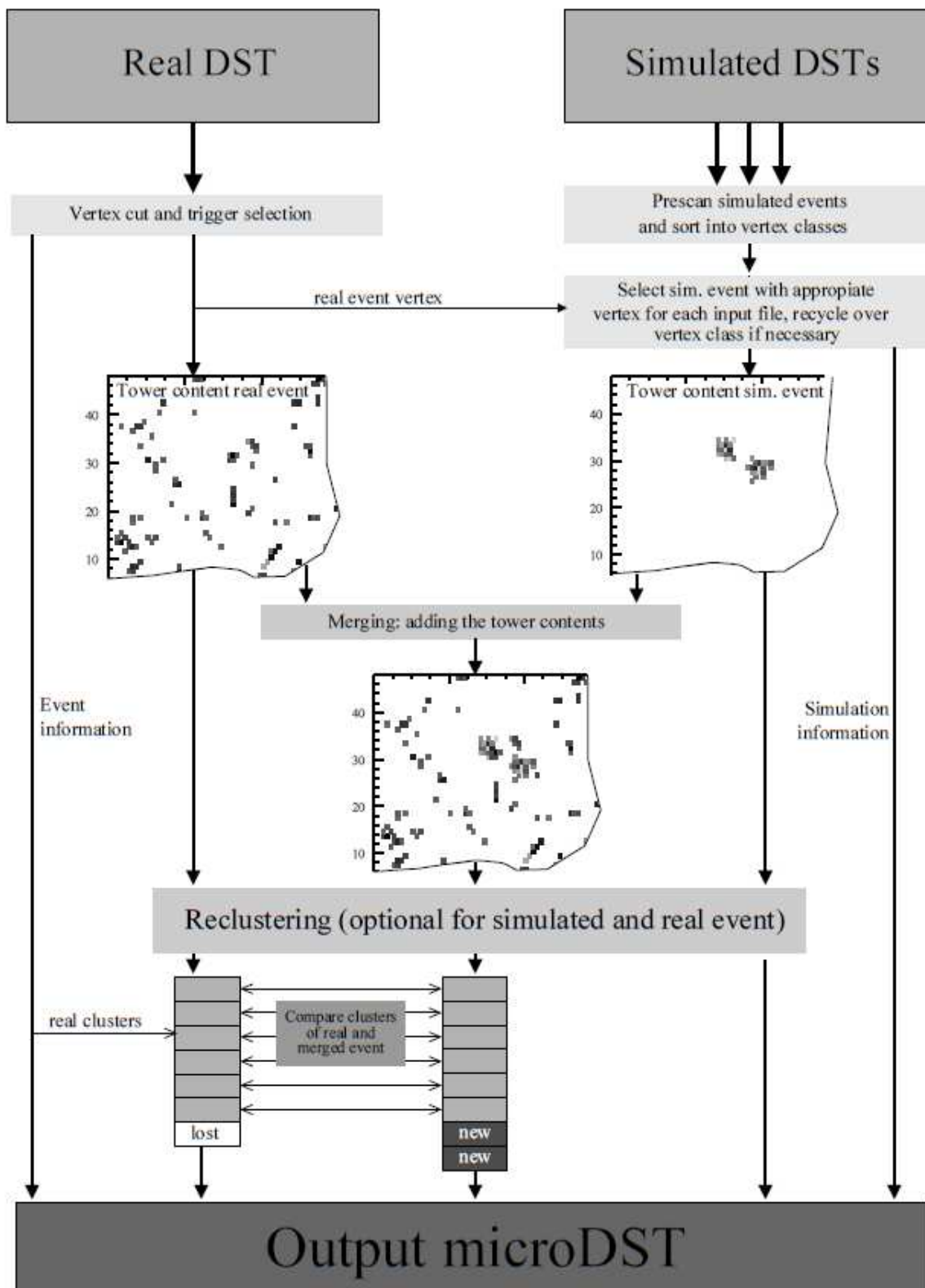


Figure 3.25: Main program flow of the embedding algorithm.

3.4.4 Inclusive Detection Efficiency

The inclusive detection efficiency for K_S^0 accounting multiplicity effect, detector geometry, response and resolution is defined as following formula;

$$\varepsilon(p_T, centrality) = \frac{dN_{K_S^0}^{reconstructed}(p_T, centrality)}{dN_{K_S^0}^{input}(p_T, centrality)} \quad (3.15)$$

where $dN_{K_S^0}^{input}(p_T, centrality)$ denotes the number of input K_S^0 with one p_T class and one centrality class. The results which involed this analysis are shown in Figure 3.26 and 3.27.

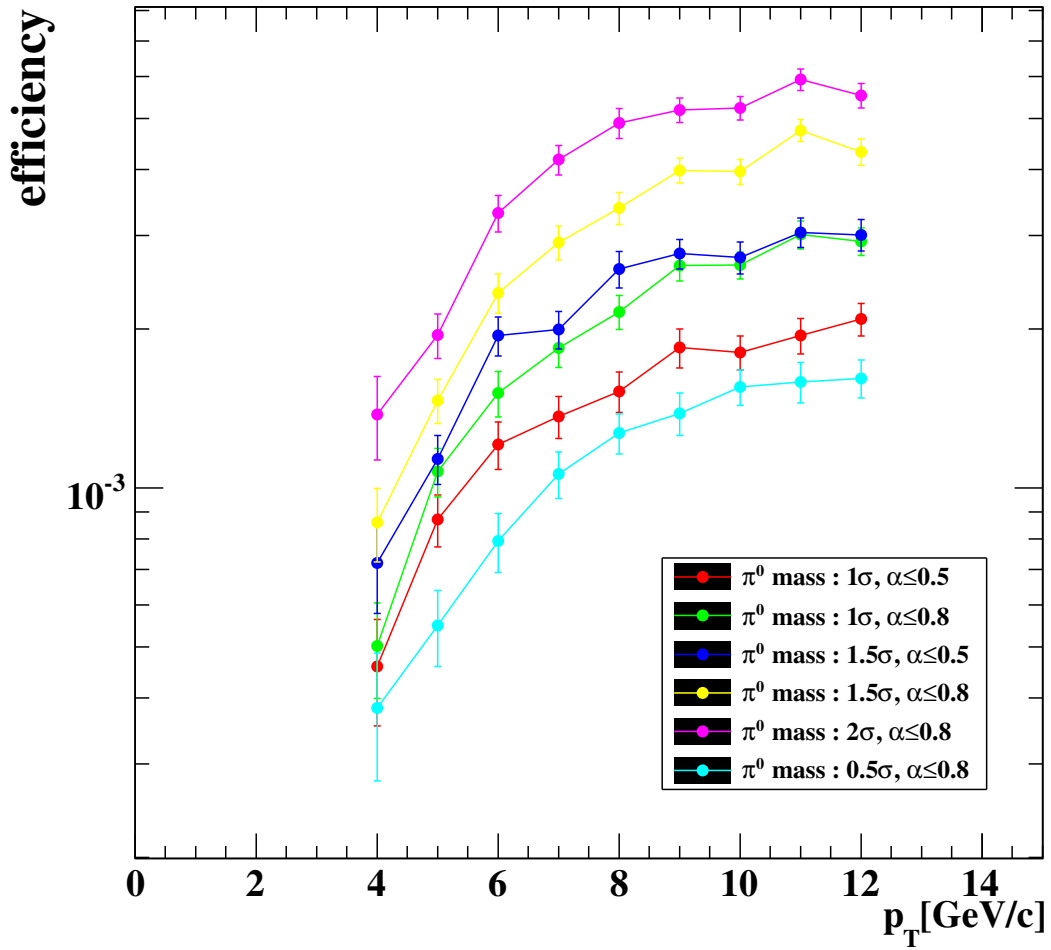


Figure 3.26: Geometrical and reconstruction efficiency calculated by embedding simulation (Centrality 0-92.2%)

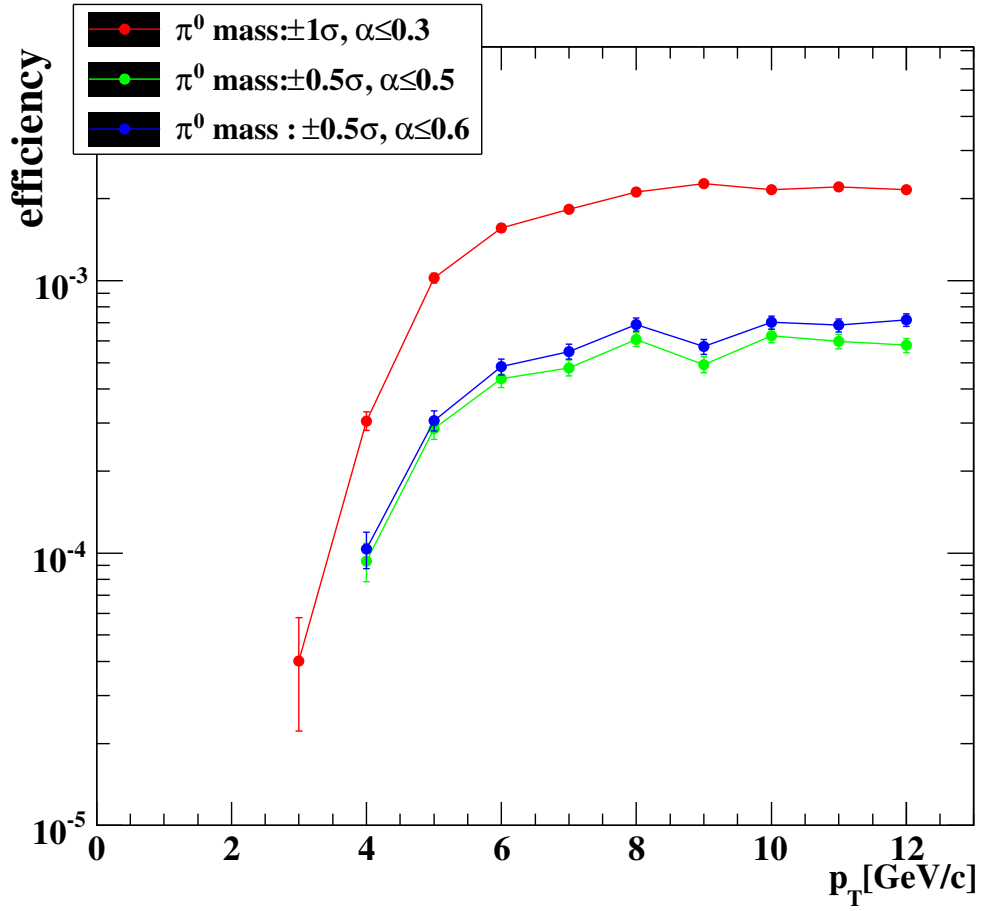


Figure 3.27: Geometrical and reconstruction efficiency calculated by embedding simulation (Centrality 60-92.2%)

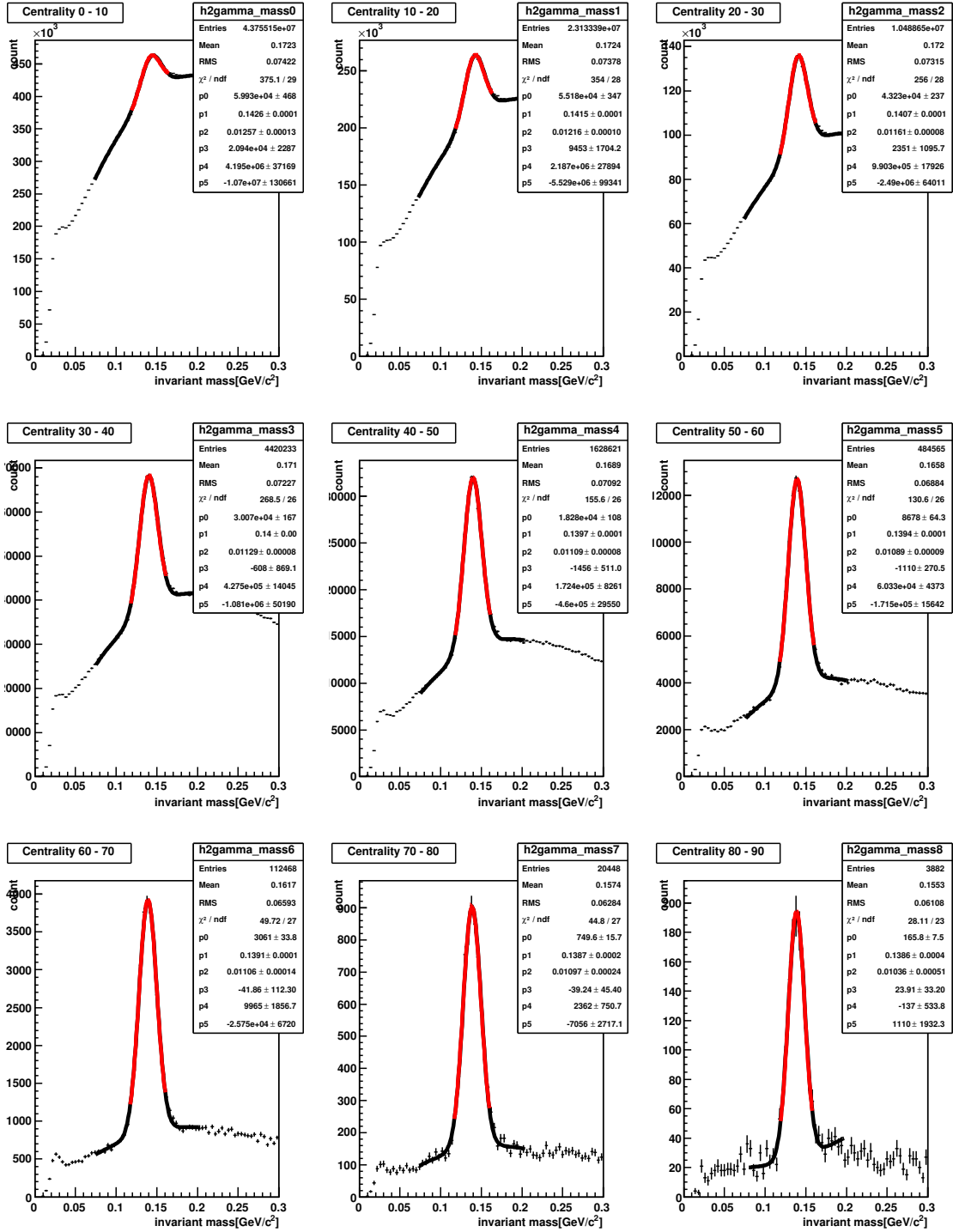


Figure 3.9: 2γ mass spectra sliced by centrality

Chapter 4

Invariant Yield and Cross Section

4.1 Introduction

Some high energy experiments are performed with a single beam focused at a stationary fixed target with the laboratory frame, that is highly Lorentz boosted. And some are collider experiments, like RHIC where detectors are generally in the center of mass frame. However some colliders like HERA run in asymmetric mode where the CM is still slightly boosted in reference to the laboratory detectors. It is therefore convenient to measure Lorentz invariant quantities. Since p_T and rapidity differences are both Lorentz invariant, the quantity

$$\frac{d^3 N}{d^2 \vec{p}_T dy} \quad (4.1)$$

is a Lorentz invariant yield, where \vec{p}_T is the momentum components in the two transverse dimensions. Since the total number of events or particles N is dependent on the effective luminosity L , which will be different experiment by experiment. So we must normalize to obtain the invariant mass cross section;

$$\begin{aligned} \frac{d^3 N}{d^2 \vec{p}_T dy} &= \frac{1}{L} \frac{d^2 \sigma}{d^2 \vec{p}_T dy} \\ &= \frac{1}{L} \frac{d^2 \sigma}{2\pi dp_T dy} \end{aligned} \quad (4.2)$$

where the last equation holds with the azimuthal symmetry. Individual Au+Au events are not azimuthally symmetric due to reaction plane dependent flow, however, when looking at the inclusive p_T spectra, we will be averaging over all reaction planes and the distributions are azimuthally isotropic. The invariant cross section can be directly compared across experiments at the same $\sqrt{s_{NN}}$ energy.

In PHENIX, minimum bias trigger is sensitive to the entire 0-92.2% central portion of the Au+Au cross section. Therefore when measuring a production in fractions within

this range, it is experimentally more accurate to normalize by the number of total events observed than by luminosity. Therefore what we present as results is are normalized invariant cross section for the various centrality fractions;

$$\frac{1}{2\pi N_{events}} \frac{d\sigma^{Au+Au \rightarrow X}}{dp_T dy} = \frac{1}{\sigma^{AuAu}} \frac{d\sigma^{Au+Au \rightarrow X}}{2\pi p_T dy} \quad (4.3)$$

4.2 Invariant Yield

The methods used to obtain the “raw” yields for K_S^0 is discussed in previous section 3.3.4. Once the raw yield is extracted from the data, a number of corrections were applied to turn them into true invariant yield equivalent to cross section measurements. For a centrality bin $cent$, the form of the correction is as follows;

$$\frac{1}{N_{cent}^{event}} \frac{1}{2\pi p_T} \frac{dN_{cent}^{K_S^0}}{dp_T dy} = \frac{1}{N_{cent}^{event}} \frac{1}{\epsilon_{cent}} \frac{dN_{cent}^{raw K_S^0}}{dp_T} \quad (4.4)$$

As we simulated K_S^0 decay in PISA, that means we allowed all decay modes, the inclusive detection efficiency ϵ includes the branching ratio of $K_S^0 \rightarrow 2\pi^0 \rightarrow 4\gamma$ decay.

4.3 Bin Shift Correction

The deviations of the data points from the true spectrum due to the finite bin size have to be corrected.

Let $f(p_T)$ denote the true K_S^0 spectrum ($dN_{K_S^0}/dp_T$, not divided by p_T yet). In this analysis, we used Levy function multiplied by p_T is used for the functional form of f .

First, fit the spectrum by f . Then, in a given bin range from p_T^{min} to p_T^{max} , we can obtain mean yield (*mean height*) of each bin by

$$(mean\ height) = \frac{1}{p_T^{max} - p_T^{min}} \cdot \int_{p_T^{min}}^{p_T^{max}} f(p_T) dp_T \quad (4.5)$$

For the next step, define ratio as following.

$$r = \frac{(mean\ height)}{f(p_T^{center})} \quad (4.6)$$

Finally, corrected yield $Y_{corrected}$ can be obtained as

$$Y_{corrected} = \frac{Y_{uncorrected}}{r} \quad (4.7)$$

In this analysis, the bin shift correction was operated 3 times iteratively.

Chapter 5

Systematic Errors

5.1 Peak Extraction

The peak extraction systematic error occurs because the “true” parameterization of the residual background is not known and is just approximated with an appropriate fit. As a background is influenced by the event multiplicity, the systematic error is larger in central collision events and it is also larger at low transverse momenta.

To estimate this contribution, we counted the number of K_S^0 by fitting several background shape functions;

- function 1 : Gaussian + constant
- function 2 : Gaussian + quadratic function
- function 3 : Gaussian + exponential
- function 4 : Gaussian + exponential + constant

5.1.1 Geometrical Acceptance of the EMCal

The error on acceptance is estimated from the misalignment of the EMCal. We calculated the change in solid angle of the fiducial volume with and without the alignment corrections. From this, uncertainty on the EMCal acceptance is 2% for single photon. Therefore, we multiply it by 4 because we measure K_S^0 via four photons.

5.1.2 Energy Scale and Nonlinearity

We define the energy scale error as an error on the spectrum (invariant yield) due to an overall multiplicative error on the energy measurement, i.e. assuming the following

relation between the measured and true energies: $E_{meas} = (1 + \epsilon)E_{true}$, which then distorts the true spectrum $f_{true}(p_T)$ to $f_{meas}(p_T) = d(\epsilon, f_{true}(p_T))f_{true}(p_T)$. If $f_{true}(p_T)$ is exponential, $d(\epsilon, f_{true}(p_T))$ is rising very fast with p_T . However, if (and only if) $f_{true}(p_T)$ is power-law, $d(\epsilon, f_{true}(p_T))$ is constant, and if the exponent of the power-law is n and the energy scale error is ϵ , the error on the invariant yield will be $(1 + \epsilon)^n$. Since the exponent of the true spectrum changes somewhat with centrality, the energy scale error has a small centrality dependence.

5.1.3 Conversion

The error on our corrections for conversion is admittedly only a cautious guess. This correction relies entirely on simulations and we found no independent way to check them. The dominant part of the correction (the shift in energy scale, $\sim 5\text{-}6\%$) relies on the simulation of electromagnetic showers which is quite reliable, accounting for the conversions themselves and the “net loss” depends on the description of the detector geometry in PISA and untestable. The net loss is about 3% , we assume that this has 1.5% absolute error to which we add linearly another 6% shift for four γ measurement.

5.1.4 Branching Ratio

Due to the error in branching ratios for both $K_S^0 \rightarrow \pi^0\pi^0$ (1.96×10^{-3}) and $\pi^0 \rightarrow 2\gamma$ (2.24×10^{-4}), we have to consider contributions from these. This contributes by 0.2% .

5.2 Summary of Systematic Errors

The summary of systematic errors is shown in Figure 5.1.

Table 5.1: Summary of systematic errors. Shown values are % unit.

p_T	independent	3	4	5	6	7	8	9	10	11
EMC geom acceptance	8									
EMC energy resolution		5.0	5.0	5.0	5.0	5.0	5.0	5.0	4.0	4.0
EMC energy scale		5.0	4.0	4.0	4.0	4.0	4.0	4.0	4.0	4.0
π^0 selection		6.0	6.0	6.0	7.0	7.0	8.0	8.0	9.0	9.0
Conversion	6.0									
Branching ratio	0.2									
Peak extraction(60-92.2)		22.0	21.0	25.0						
Peak extraction(0-92.2)					35.0	35.0	35.0	35.0	35.0	35.0
Peak extraction (Sim)	10.0									
Total		30	29	32	40	40	40	40	41	41

Chapter 6

Results and Discussion

6.1 K_S^0 Spectra

Here we present the K_S^0 spectra results. The newly introduced parameters for the identification as well as using photonic decay channel made it currently the highest p_T measurement of mesons including strangeness quark at RHIC for Au+Au collisions at $\sqrt{s_{NN}} = 200$ GeV. The pseudo-rapidity region coverage is the $-0.35 < \eta < 0.35$. The data were collected using the minimum bias trigger, counting 4.2×10^9 events.

The figure includes systematic error and statistical error. Centrality was determined according to the calculations explained in the analysis chapter, section 3.2. The invariant yields shown were calculated according to the formula in section 4.2. The results of $d^2N/dp_T dy$ can be found in Appendix C.

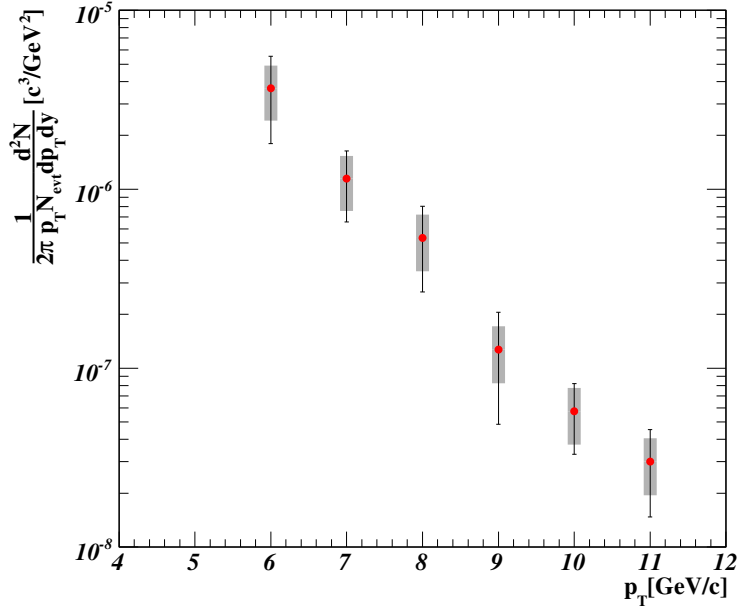


Figure 6.1: Invariant yield of K_S^0 in Au+Au Collisions at $\sqrt{s_{NN}} = 200$ GeV (Minimum Bias)

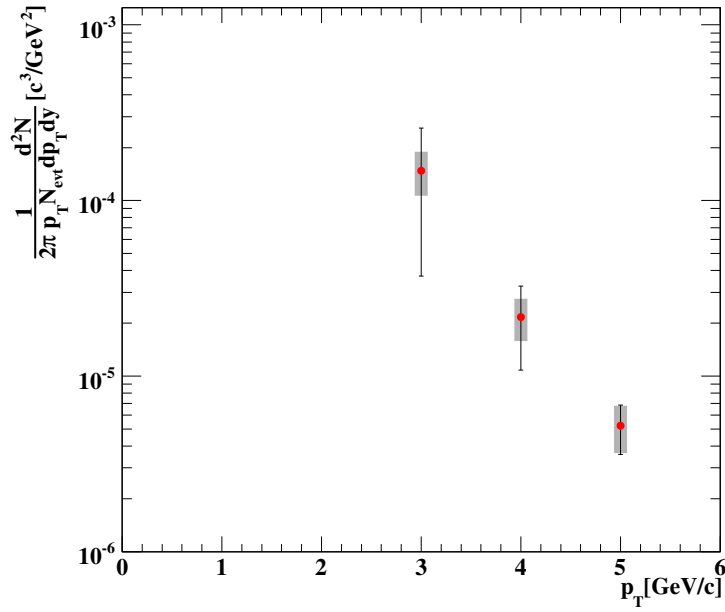


Figure 6.2: Invariant yield of K_S^0 in peripheral collisions (centrality:60-92.2%)

6.2 Medium Effect on K_S^0 meson in Au+Au Collisions at $\sqrt{s_{NN}} = 200$ GeV

6.2.1 Nuclear Modification Factor

In hot and dense medium created in the heavy ion collision, the scattered partons are expected to lose energy through gluon bremsstrahlung effectively quenching jet production as discussed in section 1.2.

To qualify medium effect, we approximate this by modeling the Au+Au collision as a sum of independent nucleon+nucleon collisions, using p+p result as a baseline.

Comparing high p_T production in Au+Au collisions and p+p is evaluated by the *nuclear modification factor*, given by ratio of the measured Au+Au invariant yield to the binary scaled p+p invariant yields;

$$R_{AA}(p_T) = \frac{(1/N_{evt}^{AA}) d^2 N_{AA}^{K_S^0} / dp_T dy}{\langle N_{coll} \rangle (1/N_{evt}^{pp}) d^2 N_{pp}^{K_S^0} / dp_T dy}$$

where $\langle N_{coll} \rangle$ is the average number of inelastic nucleon + nucleon collisions per event in each centrality bin, that is evaluated by *Glauber Monte Carlo Calculation*[26]. If medium effect is absent to hard scattering, the ratio R_{AA} will be unity ($R_{AA} = 1$); thus $R_{AA} < 1$ indicates suppression and $R_{AA} > 1$ indicates enhancement of yield. In this analysis, we used the results of the cross section of K_S^0 measured in p+p collisions at $\sqrt{s} = 200$ GeV as the reference denominator.

The yield of K_S^0 meson in Au+Au collisions at $\sqrt{s_{NN}} = 200$ GeV shows a constant suppression of factor of approximately four. On the other hand, the yield in peripheral collisions is consistent with the absence of medium effect.

These results indicate that strangeness quark loses its energy as traversing a hot and dense medium formed in the Au+Au $\sqrt{s_{NN}} = 200$ GeV collisions, even though it has about 100 times heavier mass than up quark and down quark.

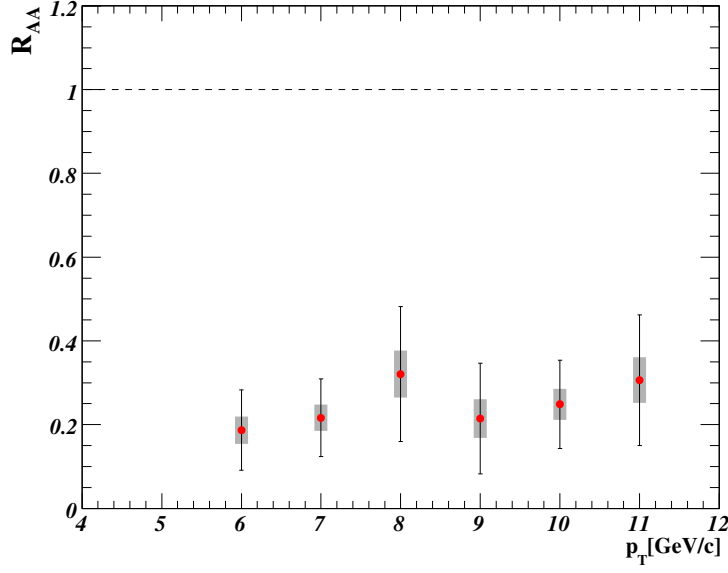


Figure 6.3: Nuclear modification factor of K_S^0 in Au+Au collisions at $\sqrt{s} = 200$ GeV

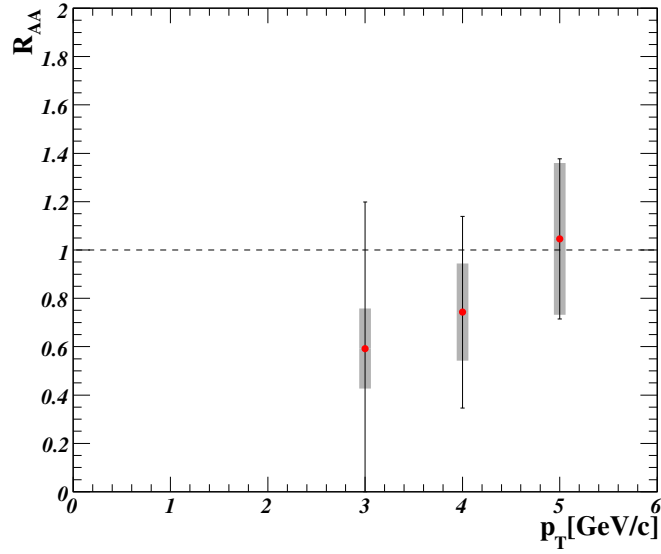


Figure 6.4: Nuclear modification factor of K_S^0 in Au+Au peripheral collisions at $\sqrt{s} = 200$ GeV

6.2.2 Comparison with Other Mesons

In this section, we compare the present result with other mesons in the context of motivation, which provides further information of parton energy loss.

Figure 6.5 shows the R_{AA} of $K_S^0, \pi^0, \eta, \omega$, and ϕ meson measured in the PHENIX experiment. K_S^0, π^0 and η shows the same amount of suppression at $p_T \geq 6$ GeV/c. Also, a vector meson ω draws the same suppression pattern with K_S^0 and others that are pseudo-scalar mesons. In addition, the suppression pattern of ϕ meson connects to that of K_S^0 meson smoothly at $p_T = 7$ GeV/c.

As a summary, the amount of suppression for $K_S^0, \pi^0, \eta, \omega$, and ϕ meson become the same value in p_T above 7 GeV/c. This indicates no existence of the flavor dependence between up, down and strangeness in this p_T range at RHIC energy.

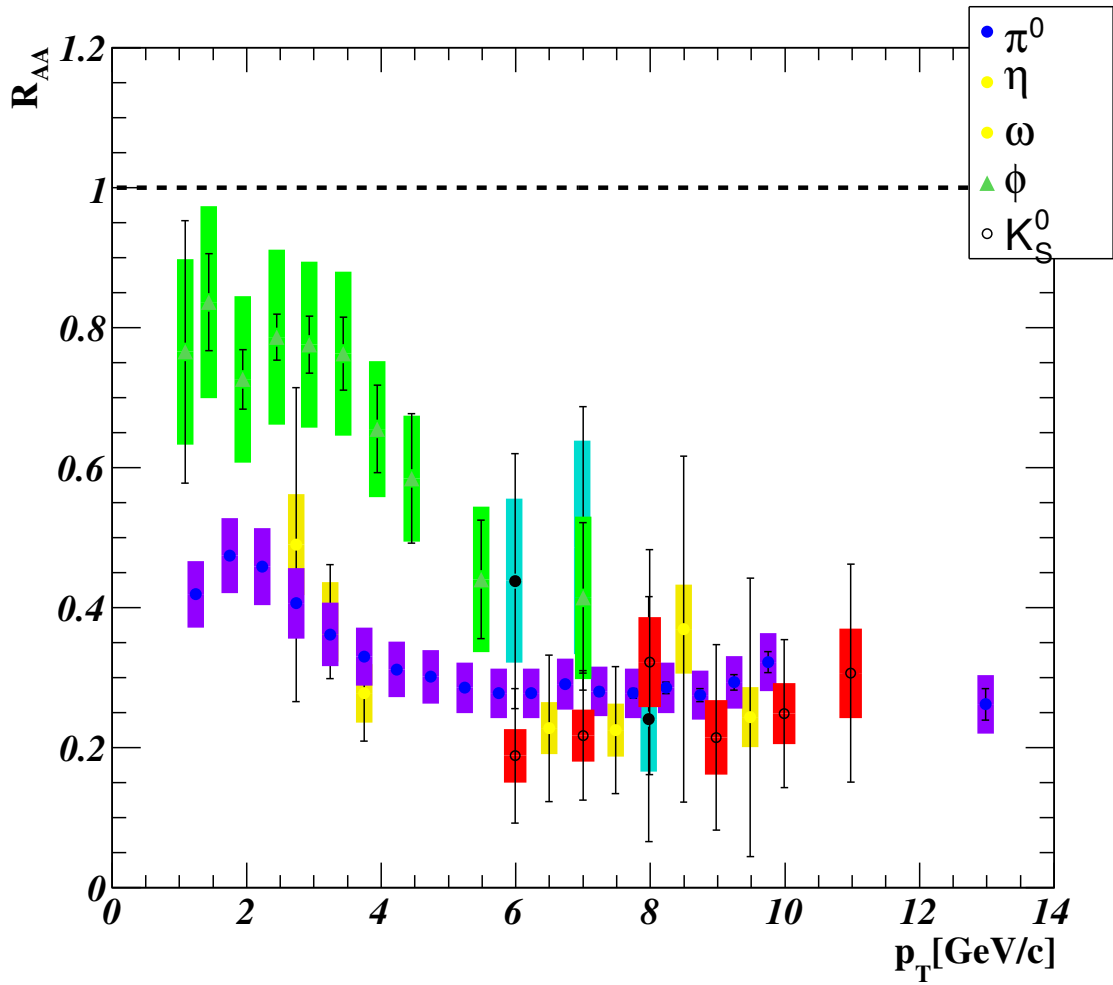


Figure 6.5: Comparison of nuclear modification factors in Au+Au $\sqrt{s} = 200$ GeV collisions (Centrality 0-92.2%)

6.2.3 Comparison with Theoretical Predictions

Figure 6.6 shows the present results and the result of model calculations of parton energy loss. The line represents GLV calculation using gluon density $dN_g/dy = 1150$ as a input parameter. The GLV calculation successfully reproduces the measured R_{AA} .

Figure 6.7 shows the theoretical calculation of nuclear modification factor for K_S^0 with and without jet conversion effect [32]. Currently, we can't judge whether the jet conversion effect is present or not due to the error, though consistent with both.

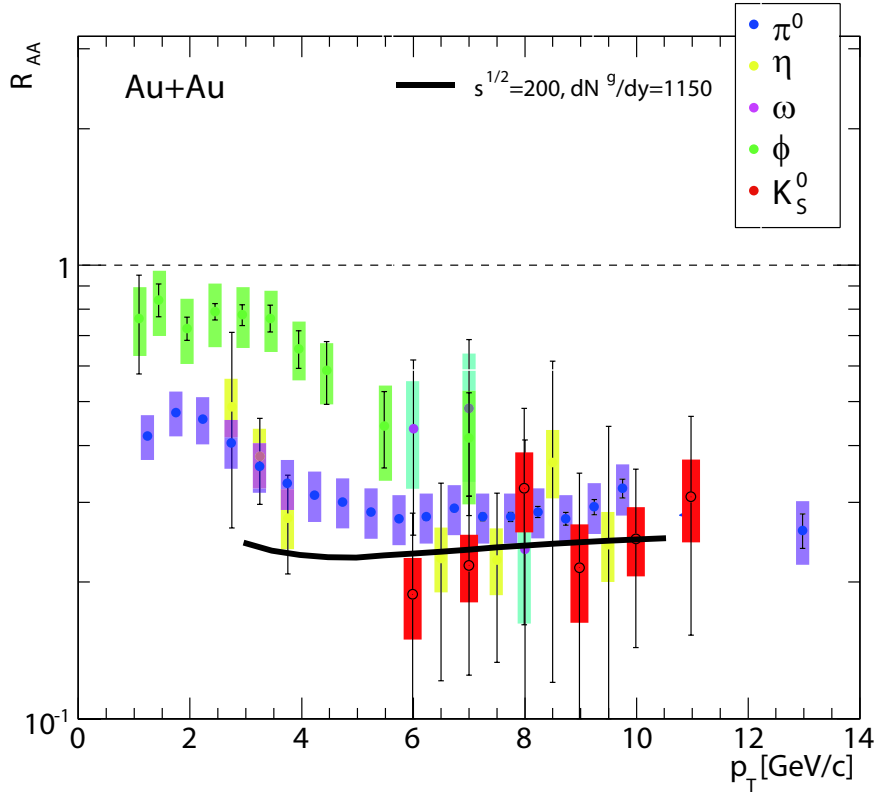


Figure 6.6: R_{AA} of mesons as a function of p_T . The black line represents GLV model calculation using gluon density $dN_g/dy = 1150$.

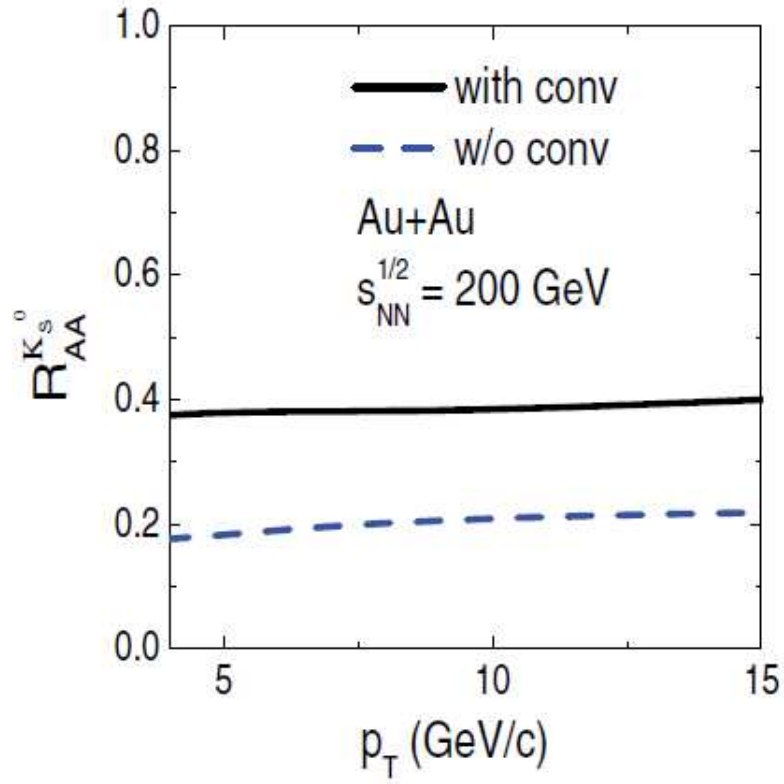


Figure 6.7: Prediction of nuclear modification factor for K_S^0 at $\sqrt{s_{NN}} = 200$ GeV Au+Au collisions with and without jet conversion effect.

Chapter 7

Conclusion

We report the first measurement of K_S^0 mesons using photonic decay mode from the Au+Au collisions at $\sqrt{s_{NN}} = 200$ GeV at the PHENIX experiment. We measured the invariant yield at p_T from 6 GeV/c to 11 GeV/c in the pseudo-rapidity coverage of -0.35 to 0.35. This is the highest p_T measurement of mesons including strangeness quark in ultra-relativistic heavy ion collisions. The data were collected using the minimum bias trigger, counting 4.2×10^9 events.

The yield of K_S^0 meson in Au+Au collisions at $\sqrt{s_{NN}} = 200$ GeV exhibits a constant suppression of a factor of four in $p_T \geq 6$ GeV/c compared to the yield in p+p reactions scaled with the corresponding number of binary nucleon-nucleon collisions in the heavy ion reaction. By contrast, the yield in peripheral collisions is consistent with the expectation provided by the scale p+p reference. This measurement brought the first observation of the flat suppression behavior of mesons including strangeness quark in heavy ion collisions at RHIC energy. Furthermore, the same amount of suppression as π^0 , η , and ω meson is observed for the first time with independent of their quark flavor composition.

These results indicate that strangeness quark also loses its energy as traversing a hot and dense color medium formed in the ultra-relativistic nuclear collisions, even though it has about a hundred times heavier mass than up quark and down quark.

Acknowledgement

I would like to thank Prof. Kenta Shigaki. His suggestion to participate in photon analysis in the PHENIX experiment was the trigger for this work. Without his vital support and advice, I couldn't succeed in this measurement. Also, he gave me a great chance to talk to Xin-Nian Wang, who is one of the foremost researchers in the field of theoretical parton energy loss. Prof. Toru Sugitate, the group leader of our laboratory gave me many chances to go to the Brookhaven National Laboratory. I could learn a really lot of things there. I thank Misaki Ouchida for teaching photon analysis and giving me advices for this work. Her measurement of ω mesons led this work. Dr. Kensuke Homma who organized Journal Club in our laboratory gave me a broader point of view about high energy physics. Dr. Hisayuki Torii and Dr. Takao Sagakuchi gave me very important suggestions that make this measurement possible. Dr. Takuma Horaguchi, the organizer of Spa Club taught me photon analysis and computing. His talk was always tickled my funny bone. I appreciate Yuji Tsuchimoto, Yoshihide Nakamiya, Kotaro M. Kijima for teaching analysis techniques and useful discussions. Their daily help was crucial for my work. Hiroyuki Harada always helped me when I facing a trouble. I'm grateful to my colleagues, Kenta Mizoguchi, Yu Maruyama and Yusuke Okada.

I thank Stefan Bathe and Ástrid Morreale for holding focus seminar, Gabor David for holding uBNL, Jeffery T. Mitchell for helping me with analysis. Wall Jack, a officer of Information Technology Division, helped me solve network trouble occurred multiple times. I appreciate Dima Ivanishchev for his work of K_S^0 measurement in p+p collisions. Without his work, I couldn't calculate R_{AA} in time for the submission. I express special thanks to Takeshi Kanetsue for vital helps at BNL and in New York City.

I sincerely appreciate my father and mother; Yukihiro and Chizuko. Without their support and encouragement, I could never do this work.

Appendix A

Kinematics

We describe the coordinate system of the PHENIX and certain kinematic variables.

A.1 Coordinate

The coordinate system for the PHENIX experiment is shown in Figure A.1. The beam axis is defined as the z axis. Components along the beam axis are called as the *longitudinal* components, while components lying x - y plane are called as the *transverse* components. ϕ is the polar angle measured from the z axis and θ is the azimuthal angle measured clockwise from the x axis.

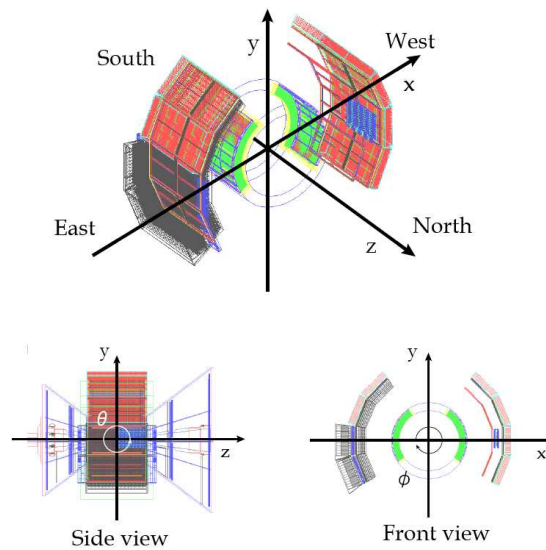


Figure A.1: Coordinate system of the PHENIX experiment

A.2 Kinematic Variables

When studying ultra-relativistic heavy ion collisions, it is useful to choose the kinematic variables in a way that they are subject to simple transformations when changing the reference frame. The relativistic energy allows to use the natural units, $c = \hbar = 1$. According to the rules of special relativity, a particle is characterized by its four-momentum;

$$P^\mu = (E, \vec{p}) = (E, p_x, p_y, p_z) \quad (\text{A.1})$$

with the energy E and the usual three-momentum of the particle \vec{p} . The absolute value of the four-momentum, called invariant mass m_{inv} , is the same in all reference frames and invariant under Lorentz transformation;

$$m_{inv}^2 = P^2 = P^\mu P_\mu = E^2 - \vec{p}^2 \quad (\text{A.2})$$

For a free particle the invariant mass is identical to its rest mass m_0 . In high energy physics the sum of the four-momenta of two colliding particles leads to the definition of the Mandelstam variable s ;

$$s = (P_1 + P_2)^2 \quad (\text{A.3})$$

with \sqrt{s} determining the center of mass energy of the reaction.

The beam is usually considered to point into the z-directions. Thus the component along the beam axis, the longitudinal momentum is defined as follow;

$$p_L = p \cos \theta \quad (\text{A.4})$$

where p is the absolute value the momentum and θ is the angle with respect to the beam axis. While the transverse momentum is given as follow;

$$p_T = \sqrt{p_x^2 + p_y^2} = p \sin \theta \quad (\text{A.5})$$

The transverse momentum p_T is invariant under Lorentz transformation in z-direction, while p_L is not invariant. Therefore the dimensionless rapidity y is defined. It is directly related to the longitudinal velocity $\beta_L = p_L/E$ of a particle;

$$y = \text{atanh} \beta_L = \frac{1}{2} \ln \left(\frac{E + p_L}{E - p_L} \right) \quad (\text{A.6})$$

It has the advantage to be additive under Lorentz transformation into a reference frame that moves at a velocity β with respect to the old reference frame in longitudinal direction;

$$y' = y + \text{atanh} \beta \quad (\text{A.7})$$

For this reason the shape of a distribution is independent of the reference frame when it is given in units in rapidity. The rapidity is connected to the energy of a particle and to its longitudinal momentum via the transverse mass $m_T = \sqrt{p_T^2 + m_0^2}$;

$$E = m_T \cdot \cosh(y) \tag{A.8}$$

$$p_L = m_T \cdot \sinh(y) \tag{A.9}$$

In the high energy limit $E \gg m_0$ the rapidity can be approximated by the pseudo-rapidity η ;

$$\eta = \frac{1}{2} \ln \left(\frac{p + p_L}{p - p_L} \right) = - \ln \left(\tan \frac{\theta}{2} \right) \tag{A.10}$$

The pseudo-rapidity is only determined by the angle θ of the particle direction of motion with respect to the beam axis. For this reason it is usually easier to determine the pseudo-rapidity than the rapidity of a particle. Similar to Equation A.8 and A.9 holds;

$$E = p_T \cdot \cosh(\eta) \tag{A.11}$$

$$p_L = p_T \cdot \sinh(\eta) \tag{A.12}$$

Appendix B

Basic Constants of K_S^0 meson

The basic PDG¹ [27] constants of K_S^0 meson are shown in the tableB.1. K_S^0 meson has a relatively long life time (for example, K_S^0 flies 52cm from vertex point at $p_T = 10$ GeV).

Table B.1: Basic constants of K_S^0
 K^0 mesons (50% K_S , 50% K_L)

mass	497.614 ± 0.024 MeV
Mean life τ	$(8.953 \pm 0.005) \times 10^{-9}$ s
$c\tau$	2.6 ± 0.5 cm
$I(J^P)$	$\frac{1}{2}(0^-)$
Decay Modes	$\pi^0\pi^0$ $(30.69 \pm 0.05)\%$
	$\pi^+\pi^-$ $(69.20 \pm 0.05)\%$
	e^+e^- $1.4 \times 10^{-5}\%$ (weak decay)

¹Particle Data Group

Appendix C

$$d^2N/dp_T dy$$

Here, we present $d^2N/dp_T dy$.

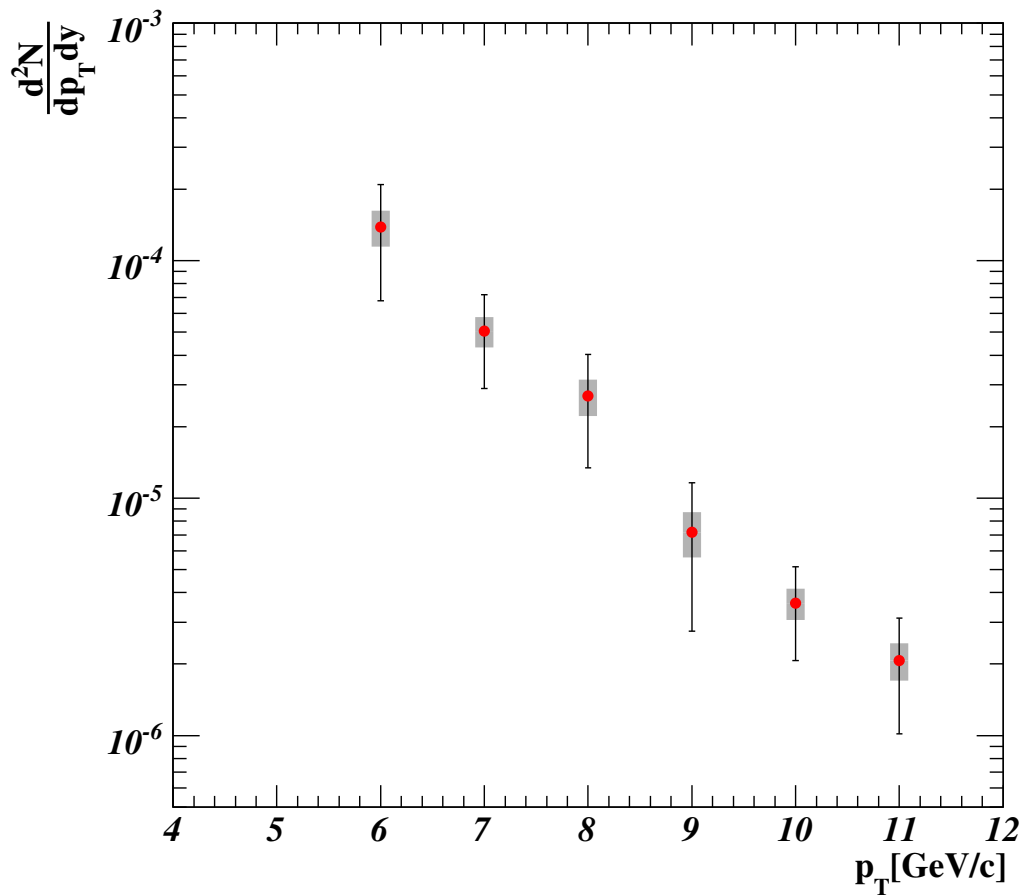


Figure C.1: p_T spectra in centrality 0-92.2%

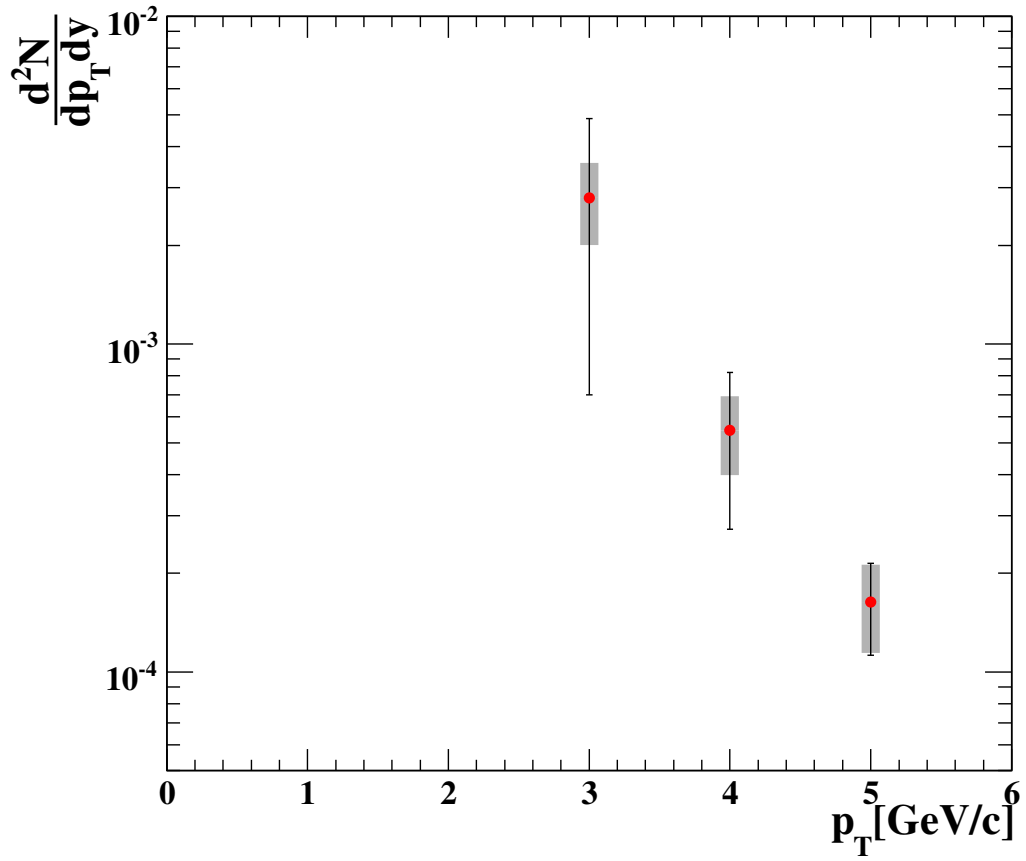


Figure C.2: p_T spectra in peripheral collisions

Appendix D

List of Analyzed Runs

228042	228145	228146	228147	228150	228152	228155	228158	228159	228164
228168	228169	228170	228171	228173	228175	228257	228258	228261	228266
228267	228272	228273	228338	228339	228341	228342	228343	228344	228396
228405	228406	228407	228408	228409	228410	228411	228474	228475	228476
228477	228478	228480	228633	229308	229309	229310	229311	229312	229492
229536	229538	229539	229541	229550	229551	229552	229553	229554	229555
229586	229587	229588	229589	229592	229594	229595	229596	229597	229650
229651	229653	229654	229656	229680	229681	229686	229687	229688	229689
229690	229691	229693	229694	229696	229697	229698	229699	229700	229701
229790	229793	229794	229796	229799	229800	229806	229808	229809	229810
229811	229812	229813	229815	229817	229818	229819	229820	229821	229902
230013	230014	230079	230080	230083	230084	230085	230086	230109	230110
230111	230112	230113	230120	230121	230122	230123	230126	230127	230128
230129	230152	230155	230159	230161	230162	230163	230170	230171	230173
230174	230175	230176	230246	230249	230251	230253	230254	230255	230256
230258	230299	230304	230305	230306	230307	230308	230309	230310	230311
230312	230313	230363	230365	230366	230367	230370	230372	230374	230456
230539	230540	230542	230543	230544	230550	230551	230554	230555	230556
230557	230658	230659	230660	230661	230662	230663	230665	230668	230669
230670	230671	230672	230673	230676	230679	230680	230682	230683	230684
230686	230800	230844	230845	230846	230847	230848	230935	230945	230947
230973	230995	230996	231154	231155	231158	231211	231218	231219	231221
231427	231429	231434	231438	231639	231640	231641	231695	231696	231697
231699	231706	231716	231717	231718	231719	231720	231721	231722	231723
231765	231766	231767	231768	231769	231770	231773	231775	231776	231777
231778	231780	231784	231786	231796	231800	231811	231821	231876	231877
231878	231880	231881	231920	231921	231922	231931	231932	231933	231992
231993	231996	231997	232000	232003	232004	232005	232006	232011	232012
232014	232020	232021	232377	232378	232379	232381	232382	232383	232384
232457	232458	232459	232460	232461	232462	232463	232464	232465	232599

232600	232601	232602	232603	232610	232611	232612	232613	232616	232617
232618	232619	232620	232805	232806	232807	232810	232823	232824	232825
232828	232829	232830	232831	232837	232839	232871	232872	232992	232996
233000	233001	233002	233004	233005	233006	233007	233010	233013	233015
233016	233017	233018	233019	233020	233022	233025	233027	233141	233164
233165	233170	233172	233278	233279	233280	233281	233282	233283	233284
233286	233287	233296	233297	233306	233307	233308	233379	233381	233382
233385	233388	233394	233395	233396	233398	233415	233474	233475	234139
234142	234143	234175	234202	234416	234441	234449	234457	234522	234523
234524	234525	234526	234571	234572	234574	234667	234673	234674	234682
234685	234686	234687	234688	234690	234746	234757	234869	234871	234872
234873	234876	234878	234879	234880	234881	234887	234889	234891	234896
234898	235032	235050	235051	235223	235226	235227	235228	235229	235231
235232	235235	235238	235242	235244	235363	235364	235365	235366	235390
235391	235397	235526	235529	235531	235532	235551	235553	235554	235555
235559	235563	235567	235568	235569	235570	235571	235572	235573	235613
235616	235656	235657	235658	235659	235660	235683	235684	235685	235686
235690	235691	235695	235696	235698	235699	235700	235794	235795	235796
235797	235798	235800	235801	235802	235804	235805	235807	235809	235895
235900	235901	235902	236004	236005	236007	236008	236009	236133	236134
236135	236136	236245	236246	236247	236248	236258	236259	236260	236379
236380	236381	236382	236385	236390	236394	236395	236398	236399	236400
236401	236402	236403	236404	236406	236407	236409	236413	236416	236418
236419	236420	236421	236463	236464	236465	236466	236467	236505	236506
236521	236522	236523	236524	236536	236538	236539	236540	236605	236666
236778	236779	236780	236782	236784	236786	236794	236803	236804	236805
236903	236949	236950	236952	237090	237091	237093	237099	237101	237102
237232	237233	237235	237270	237356	237360	237733	237751	237815	237822
237830	238031	238136	238137	238143	238148	238149	238170	238171	238327
238330	238331	238332	238338	238339	238518	238536	238655	238943	238944
238947	238961	238966	238967	238968	238970	238975	239307	239309	239311
239320	239321	239323	239324	239326	239418	239441	239442	239461	239464
239465	239466	239467	239471	239472	239473	239474	239475	239476	239542
239543	239600	239601	239608	239609	239610	239611	239612	239658	239659
239660	239666	239668	239669	239670	239741	239755	239756	239758	239759
239760	239772	239777	239778	239779	239817	239820	239834	239839	239840
239841	239843	239909	239912	239914	239916	239917	239918	239919	239922
239923	239924	239925	239926	239927	239933	239936	239937	239949	239950
239951	240041	240042	240043	240044	240048	240049	240053	240054	240055
240058	240059	240060							

Table D.1: List of Analyzed Runs

Bibliography

- [1] S. S. Adler *et al.* Phys. Rev. Lett. **96**, 202301 (2006).
- [2] S. S. Adler *et al.* Phys. Rev. Lett. **91**, 072301 (2003).
- [3] K. Adcox *et al.* Phys. Lett. B **561**, 82 (2003).
- [4] K. Adcox *et al.* Phys. Rev. Lett. **88**, 022301 (2002).
- [5] Phys. Rev. Lett. **96**, 202301 (2006).
- [6] M. Gyulassy, P. Levai and I. Vitev, Phys. Lett. **594**, 371 (2001).
- [7] S. Eidelman *et al.* [Particle Data Group], Phys. Lett. B **592**, 1 (2004). (URL: <http://pdg.lbl.gov>)
- [8] S. Weinberg, Phys. Rev. Lett. **31** (1973) 494, H. Fritzsche, M. Gell-Mann and H. Leutwyler, Phys. Lett. **47B** (1973) 365, D. J. Gross, F. Wilczek, Phys. Rev. **D8** (1973) 3633
- [9] L. D. Landau and I. J. Pomeranchuk, Dokl. Akad. Nauk. SSSR **92** (1953) 92; A. B. Migdal, Phys. Rev. **103** (1956) 1811
- [10] K. Kasahara, Phys. Rev. **D31** (1985) 2737
- [11] E146 collaboration: P. L. Anthony *et al.* Phys. Rev. **D56** (1997) 1373
- [12] S. J. Brodsky and J. F. Gunion, Phys. Rev. **D17** (1978) 848
- [13] R. Baier, Yuri L. Dokshitzer, S. Peigne, D. Schiff, Phys. Lett. **B345** 277-286 (1995)
- [14] X. N. Wang, M. Gyulassy, M. Plumer. Phys. Rev. **D51** 3436-3446 (1995)
- [15] R. Baier, Y. L. Dokshitzer, A. H. Mueller, *et al.*, Nucl. Phys. **B483** (1997) 291.
- [16] Xin-Nian Wang and Miklos Gyulassy. Phys. Rev. **D44** 3501-3516 (1991)

- [17] J. F. Gunion and G. Bretsch, Phys. Rev. **D25** (1982) 746
- [18] M. Gyulassy and X. N. Wang, Nucl. Phys. **B420** (1994) 583
- [19] X. N. Wang, Phys. Rev. **C55** (1997) 3047
- [20] R. Baier *et al.*, Phys. Lett. **B345** (1995) 277
- [21] R. J. Glauber and G. Matthiae, Nucl. Phys. **21** (1970) 135
- [22] H.Hahn *et al.* Nucl. Instrum. Meth. A **499**, 245 (2003)
- [23] Y.Aramaki *et al.* PHENIX internnal Analysis Note 700 (2007).
- [24] A. V. Bazilevsky, V. I. Kochetkov, V. K. Semenov, et al. Instrum. Exp. Tech. **42** (1999) 167.
- [25] A. Bazilevsky and M. Volkov. PbSc reconstruction routine EmcScSector.cxx Rev. 2.10. PHENIX CVS Repository offline/packages/emc, 2003.
- [26] Klaus Reyger. Glauber Monte Carlo Calculations for Au+Au Collisions at $\sqrt{s_{NN}} = 200$ GeV, PHENIX internal Analysis Note (2003).
- [27] S. Eidelman *et al.* [Particle Data Group], Phys. Lett. B **592**, 1 (2004). (URL: <http://pdg.lbl.gov>)
- [28] C.Roland *et al.* J. Phys. G30 (2004) S1381-S1384
- [29] S.S.Adler *et al.* Phys. Rev. Lett. **91**, 072301 (2003).
- [30] G. David *et al.* IEEE Trans. Nucl. Sci. **42**, (1995) 306.
- [31] G. Bathow *et al.* Nucl. Phys. B **20**, (1970) 592.
- [32] W. Liu and R. J. Fries Phys. Rev. C **77**, 054902 (2008)